

“Sparse + Low-Rank” Tensor Completion Approach for Recovering Images and Videos

Chenjian Pan¹ and Chen Ling¹ and Hongjin He² and Liqun Qi^{3,4} and Yanwei Xu³

¹Department of Mathematics, School of Science, Hangzhou Dianzi University, Hangzhou, 310018, China.

² School of Mathematics and Statistics, Ningbo University, Ningbo 315211, China.

³Theory Lab, Central Research Institute, 2012 Labs, Huawei Technologies Co., Ltd., Shatin, New Territory, Hong Kong, China.

⁴Department of Applied Mathematics, The Hong Kong Polytechnic University, Hung Hom, Kowloon, Hong Kong, China.

Recovering color images and videos from highly undersampled data is a fundamental and challenging task in face recognition and computer vision. By the multi-dimensional nature of color images and videos, in this paper, we propose a novel tensor completion approach, which is able to efficiently explore the sparsity of tensor data under the discrete cosine transform (DCT). Specifically, we introduce two “sparse + low-rank” tensor completion models as well as two implementable algorithms for finding their solutions. The first one is a DCT-based sparse plus weighted nuclear norm induced low-rank minimization model. The second one is a DCT-based sparse plus p -shrinking mapping induced low-rank optimization model. Moreover, we accordingly propose two implementable augmented Lagrangian-based algorithms for solving the underlying optimization models. A series of numerical experiments including color image inpainting and video data recovery demonstrate that our proposed approach performs better than many existing state-of-the-art tensor completion methods, especially for the case when the ratio of missing data is high.

Index Terms—Tensor completion, p -shrinkage thresholding, weighted nuclear norm, discrete cosine transform, image inpainting.

I. INTRODUCTION

WITH the rapid developments of sensor technologies and video surveillance systems, the collected images and videos are naturally stored as multi-way arrays, which are also called tensors. As we know, the complete information of images and videos is very important to make a good decision for intelligent devices or data users. However, during the acquisition process, observed image and video data often contain missing entries (or pixels). In this situation, estimating these missing information of images and videos, which is also called tensor completion, is a fundamental and challenging problem in the communities of image processing and computer vision, e.g., see [1]–[4] and references therein.

It is well-known that tensor is a higher-order extension of matrix, so the tensor completion is also a natural generalization of matrix completion. Generally speaking, when the missing entries are sparse in an incomplete matrix, we could efficiently explore the local information around the unknown components to get a relatively ideal completion to the matrix, e.g., see [5]–[7]. However, when dealing with a highly undersampled matrix, it is incredibly difficult, even if not impossible, to accurately estimate these missing entries from an incomplete matrix without any global or prior information. Comparatively, the complex structure of tensors makes that recovering the missing entries from a highly undersampled tensor puts forward more theoretical and computational challenges at the interface of statistics and optimization, e.g., see [8]. In the past decades, it is well-documented that exploiting the inherent global information, e.g., low-rank and sparsity, of the data is able to greatly improve the estimation quality of highly

undersampled matrices and tensors, e.g., see [9]–[13], to name just a few.

As a direct extension of the low-rank matrix completion, the canonical *low-rank tensor completion* (LRTC) model is expressed mathematically as

$$\begin{aligned} \min_{\mathcal{X}} \quad & \text{rank}(\mathcal{X}) \\ \text{s.t.} \quad & \mathcal{P}_{\Omega}(\mathcal{X}) = \mathcal{P}_{\Omega}(\mathcal{H}), \end{aligned} \quad (1)$$

where both \mathcal{X} and \mathcal{H} are N -th order tensors, $\text{rank}(\cdot)$ denotes the rank function, Ω is the index set corresponding to the observed entries of the incomplete tensor \mathcal{H} , and $\mathcal{P}_{\Omega}(\cdot)$ is the linear operator that keeps known elements in Ω while setting the others to be zeros. It has been documented in [14], [15] that directly minimizing the rank function of tensors, even for matrices, is an NP-hard problem. Moreover, unlike the unique definition of rank for matrices, there are diverse definitions for tensors such as CANDECOMP/PARAFAC (CP) rank, Tucker rank and Tensor Train (TT) rank (see [16], [17]). Consequently, the diversity of tensor ranks often makes engineers difficult to choose an appropriate surrogate for characterizing the low-rankness of their problems.

Roughly speaking, most state-of-the-art tensor completion methods can be grouped into two categories. (i) The first type refers to the tensor nuclear norm minimization approach, which unfolds the underlying tensor as a series of matrices so that we could efficiently employ the matrix nuclear norm as an approximation to the rank of a tensor. Therefore, many efficient algorithms tailored for matrix completion could be naturally extended to tensor completion based on the so-called tensor nuclear norm definitions, e.g., see [9], [11], [18]–[23] and references therein. Mathematically, a seminal tensor nuclear norm minimization model introduced in [9] takes the

form

$$\begin{aligned} \min_{\mathcal{X}} \quad & \sum_{n=1}^N \alpha_n \|X_{(n)}\|_* \\ \text{s.t.} \quad & \mathcal{P}_{\Omega}(\mathcal{X}) = \mathcal{P}_{\Omega}(\mathcal{H}), \end{aligned} \quad (2)$$

where $\alpha_n \geq 0$ ($n \in [N] := \{1, 2, \dots, N\}$) can be regarded as weight parameters often satisfying $\sum_{n=1}^N \alpha_n \approx 1$, matrix $X_{(n)}$ corresponds to the mode- n unfolding of tensor \mathcal{X} for every $n \in [N]$, and $\|\cdot\|_*$ represents the well-known nuclear norm referring to the sum of all singular values of a matrix. Note that a vector consisting of the ranks of unfolding matrices $X_{(n)}$'s ($n = 1, 2, \dots, N$) is called the Tucker rank of the tensor \mathcal{X} (see [16]). Hence, the objective function in (2) is indeed a convexly weighted sum of the components of Tucker rank. Compared with the direct vectorization and matricization approaches for tensor data, model (2) efficiently exploits the multi-mode structure, thereby possibly achieving a better approximation to the low-rankness of tensor data. Moreover, these unfolding completion models (i.e., tensor nuclear norm minimization models) are beneficial for algorithmic design due to the convexity of tensor nuclear norm functions. Recently, the state-of-the-art *alternating direction method of multipliers* (ADMM) and Douglas-Rachford splitting method have been successfully applied to tensor completion, e.g., see [9], [10], [24]–[26]. (ii) The second type of tensor completion approach is based on tensor decomposition. Actually, we observe that many tensor nuclear norm based models utilize the so-called unfolding (or matricization) technique. However, Yuan and Zhang [27] showed that the matricization for higher-order tensors ignores the nature of tensors and potentially destroys some inherent properties of the data, thereby leading to suboptimal procedure, which encourages researchers to develop new completion methods from tensor decomposition perspectives. In the literature, some popular tensor decomposition techniques include CP decomposition, Tucker decomposition [16], T-SVD [28] and Tensor-Train decomposition [17]. Like the matrix decomposition, the aforementioned tensor decomposition forms have also been verified as powerful dimensionality reduction tools, which can promote the low-rankness of tensor data to some extent. Empirically, these tensor decomposition based completion models have received great successes in big data analysis, pattern recognition, and traffic data recovery, e.g., see [12], [13], [29]–[34] and references therein.

When regarding color images and videos as general tensors, the aforementioned tensor completion approaches are certainly applicable to images and video inpainting problems. However, it often fails to achieve an ideal restoration quality for highly undersampled image data since only the low-rank property is exploited in general tensor completion models (see Figs. 4 and 6). As we know, the *total variation* (TV) regularization (see [35]) is a widely used tool in the community of image processing to preserve sharp discontinuities (edges) of an image, while removing noise and other unwanted fine scale detail. Hence, researchers judiciously incorporated TV regularization into low-rank tensor completion models for the purpose of exploiting the inherent structure of images. The promising numerical performance can be found in recent works, e.g., [22], [33], [36]–[40]. From the mathematical modeling perspective, the underlying images usually are sparse

under the TV transform. Consequently, we see that an ℓ_1 -norm is used to promote the sparsity of an image in the TV transform domain, which demonstrates that combining the low-rank and TV-based sparse prior information simultaneously can greatly improve the restoration quality. However, as stated in [41], the traditional TV regularizer is still not perfect, since it only guarantees an estimation presenting a locally smooth visualization, while ignoring the global perception and structure. Such a drawback motivates us to find new sparse surrogates to recover more accurate data. Actually, in the image processing literature, the well-known *discrete cosine transform* (DCT) has been widely used for the most popular image compression standard JPEG, since DCT is powerful to obtain a (at least approximately) sparse representation of an image. For example, we consider a widely used gray video, i.e., **sidewalk** (see Fig. 1), which is a third order tensor of size $220 \times 352 \times 30$. By performing DCT on each dimension of such a gray video, a large number of elements of approach to zeros, thereby leading to a high level sparsity when setting a truncated number (TN), e.g., 0.05 and 0.1, to drop all values less than such a TN. However, the video recovered directly from the truncated tensor is still close to the original one, which means that a small sample information is possible to recover an ideal (at least identifiable) one. Such an experimental observation also encourages us to consider a sparsity regularization on the coefficient tensor under the DCT procedure. Here, we refer the reader to [41]–[47] for recent applications of DCT on image recovery and some completion methods considering the property of the tensor data in transformed domains, e.g., see [18], [48]–[50]. Compared to the TV-based tensor completion model, to the best of our knowledge, DCT-based approaches received much less considerable attention on color images and videos inpainting from tensor completion angle. Hence, we are motivated to make a further study on showing the ability of the DCT technique for recovering images and videos from highly undersampled data.

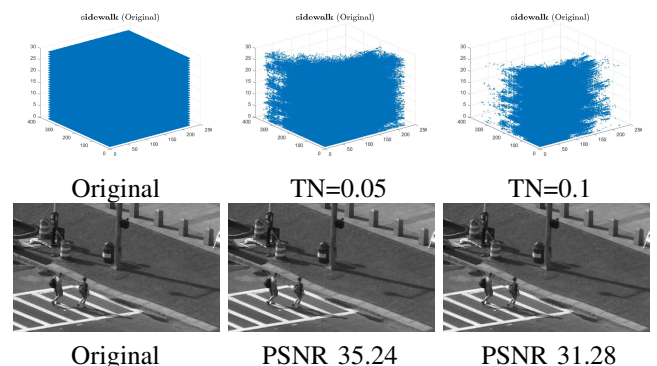


Fig. 1. The first row show the visualization of the sparsity of the gray video **sidewalk** under DCT, where the white represents 0. The second row illustrates the comparisons of the 10-th frame of the original video and the frames reconstructed from the truncated tensor.

In this paper, we introduce two “sparse + low-rank” tensor completion approaches for recovering color images and videos. Our contribution is four-fold.

- Most nuclear norm based tensor completion models equally treat all singular values of the unfolding matrices.

For some real-world data sets, small singular values are often sensitive to the incomplete (or corrupted by noise) observed information, thereby possibly leading to a suboptimal low-rank tensor. In this situation, we will propose a minimization model, whose objective function is the sum of a DCT-based sparse regularization term and a weighted nuclear norm induced low-rank regularization term so that the singular values have different weights to enhance the global low-rank structure.

- In many unfolding approaches, the most popular low-rank surrogate of tensors is the nuclear norm of unfolding matrices. Recently, both theoretical and empirical results show that the so-called p -shrinkage thresholding algorithm outperforms the classical iterative soft thresholding algorithm induced by nuclear norm for low-rank and sparse recovery problems, e.g., see [51]–[53]. Accordingly, the second contribution of this paper is that we introduce a nonconvex optimization model, which minimizes the sum of a DCT-based sparse term and a p -shrinking mapping induced low-rank term.
- We develop two implementable augmented Lagrangian-based algorithms for the proposed tensor completion models, where all subproblems of our algorithms have closed-form solutions.
- We conduct a series of experiments on color images and surveillance videos. Our computational results demonstrate that our proposed “sparse + low-rank” tensor completion approaches outperform many state-of-the-art model-driven tensor completion methods, especially for highly undersampled cases.

The structure of this paper is as follows. In Section II, we summarize some notations and recall some basic definitions including (weighted) nuclear norm of matrices, p -shrinkage mapping and proximal operators. In Section III, we will first introduce a unified “sparse + low-rank” tensor completion approach. Then, we split this section into two parts and propose two kinds of “sparse + low-rank” tensor completion models, respectively. Based on the augmented Lagrangian function, we also propose two implementable algorithms for the underlying tensor completion models. Numerically, in Section IV, we conduct the performance of our approaches on images and videos recovery from highly undersampled data. Finally, some concluding remarks are provided in Section V.

II. NOTATIONS AND PRELIMINARIES

In this section, we summarize some notations and definitions on p -shrinkage mapping and weighted nuclear norm that will be used throughout this paper.

Tensor is a multidimensional array, which is an extension of matrix. The space of all N -th order real tensors is denoted by $\mathbb{R}^{I_1 \times I_2 \times \dots \times I_N}$, where the order of a tensor is also called way or mode. Given an N -th order $\mathcal{A} \in \mathbb{R}^{I_1 \times I_2 \times \dots \times I_N}$, we denote the (i_1, i_2, \dots, i_N) -th component of \mathcal{A} by $a_{i_1 i_2 \dots i_N}$. So the N -th order tensor \mathcal{A} is also denoted by $\mathcal{A} = (a_{i_1 i_2 \dots i_N})$. Throughout this paper, tensors of order $N \geq 3$ are denoted by calligraphical letters, e.g., $\mathcal{A}, \mathcal{B}, \dots$. Generally, we use capital letters (e.g., A, B, \dots), boldfaced lowercase letters

(e.g., $\mathbf{a}, \mathbf{b}, \dots$), and lowercase letters (e.g., a, b, \dots) to denote matrices, vectors, and scalars, respectively. For any two N -th order real tensors $\mathcal{A} = (a_{i_1 i_2 \dots i_N})$ and $\mathcal{B} = (b_{i_1 i_2 \dots i_N})$, the inner product between \mathcal{A} and \mathcal{B} is given by

$$\langle \mathcal{A}, \mathcal{B} \rangle := \sum_{i_1, i_2, \dots, i_N} a_{i_1 i_2 \dots i_N} b_{i_1 i_2 \dots i_N}.$$

Consequently, the Frobenius norm of tensor \mathcal{A} associated with the above inner product is given by $\|\mathcal{A}\|_F = \sqrt{\langle \mathcal{A}, \mathcal{A} \rangle}$. Given an N -th order tensor \mathcal{A} , the mode- n matricization (or unfolding) of \mathcal{A} is denoted by $A_{(n)}$, and the (i_1, i_2, \dots, i_N) -th entry of tensor \mathcal{A} is mapped to the (i_n, j) -th entry of matrix $A_{(n)}$ in the lexicographical order, where

$$j = 1 + \sum_{1 \leq l \leq N, l \neq n} (i_l - 1) J_l \quad \text{with} \quad J_l = \prod_{1 \leq t \leq l-1, t \neq n} I_t.$$

Given a matrix $A \in \mathbb{R}^{m \times n}$, we write its *singular value decomposition* (SVD) as $A = U \Lambda V^\top$, where U and V are orthogonal matrices and Λ is a diagonal matrix, i.e.,

$$\Lambda = \text{diag}(\sigma(A)) = \text{diag}(\sigma_1(A), \sigma_2(A), \dots, \sigma_r(A))$$

with $r := \min\{m, n\}$, and the diagonals $\sigma_i(A)$'s are singular values of A satisfying $\sigma_1(A) \geq \sigma_2(A) \geq \dots \geq \sigma_r(A)$ without loss of generality. With the above preparation, we first recall the definition of (weighted) nuclear norm of a matrix (see [43]).

Definition 2.1. For any given matrix $A \in \mathbb{R}^{m \times n}$, its nuclear norm is defined by

$$\|A\|_* = \sum_{i=1}^r \sigma_i(A)$$

and the weighted nuclear norm is given by

$$\|A\|_{*, \mathbf{w}} = \sum_{i=1}^r w_i \sigma_i(A)$$

where $r := \min\{m, n\}$ and $\sigma_i(A)$ is the i -th largest singular value of A , and $\mathbf{w} = (w_1, \dots, w_r)$ is a weight vector, which, as suggested in [19], is given by

$$w_i = \delta / (\sigma_i(A) + \epsilon), \quad i = 1, 2, \dots, r,$$

where $\delta \in \mathbb{R}_+$ is a constant and ϵ is a small positive number to avoid division by 0. In algorithmic implementation, we can iteratively update w_i 's.

Below, we recall the p -shrinkage mapping introduced in [52].

Definition 2.2. Given $\mathbf{a} \in \mathbb{R}^n$, $\mu > 0$ and $p \leq 1$, the p -shrinkage thresholding operator is defined in component-wise by

$$\text{pshrink}(\mathbf{a}, \mu, p) = \text{sign}(\mathbf{a}) \odot \max\{|\mathbf{a}| - \mu |\mathbf{a}|^{p-1}, 0\}, \quad (3)$$

where ‘ $\text{sign}(\cdot)$ ’ and ‘ $|\cdot|$ ’ are the sign function and absolute value function in component-wise, respectively, and ‘ \odot ’ represents the component-wise product between two vectors. In particular, when setting $p = 1$, the p -shrinkage operator (3) immediately reduces to the well-known soft-thresholding,

which is denoted by

$$\text{shrink}(\mathbf{a}, \mu) = \text{sign}(\mathbf{a}) \odot \max\{|\mathbf{a}| - \mu, 0\}. \quad (4)$$

Clearly, the smaller p is, the less $\text{shrink}(\mathbf{a}, \mu, p)$ shrinks large inputs. We refer the reader to [53] for an illustration to the philosophy of the p -shrinkage operator.

For any given $\mathbf{a} \in \mathbb{R}^n$, the proximal operator associated with $\theta : \mathbb{R}^n \rightarrow \mathbb{R}$ about $\tau > 0$ is defined as

$$\text{prox}_{\theta, \tau}(\mathbf{a}) := \arg \min_{\mathbf{x} \in \mathbb{R}^n} \left\{ \theta(\mathbf{x}) + \frac{\tau}{2} \|\mathbf{x} - \mathbf{a}\|^2 \right\}.$$

Consequently, as shown in [54, Theorem 4] (see also [55]), for any $\mu > 0$, $A \in \mathbb{R}^{m \times n}$ and a weight vector \mathbf{w} , the global optimal solution to the following optimization problem

$$\min_X \|X\|_{*, \mathbf{w}} + \frac{1}{2\mu} \|X - A\|_F^2$$

is given by the weighted SVD thresholding

$$X^* = U \mathbf{w} \text{shrink}(\Lambda, \mu, \mathbf{w}) V^\top,$$

where $A = U \Lambda V^\top$ is the SVD of A and

$$\mathbf{w} \text{shrink}(\Lambda, \mu, \mathbf{w}) = \max\{\sigma(A) - \mu \mathbf{w}, 0\}. \quad (5)$$

Moreover, it follows from [51] that the p -shrinkage mapping defined in Definition 2.2 can also be interpreted as the proximal operator of a penalty function $\Phi_p^\mu(\cdot) : \mathbb{R}^n \rightarrow \mathbb{R}$, i.e.,

$$\mathbf{pshrink}(\mathbf{a}, \mu, p) = \arg \min_{\mathbf{x} \in \mathbb{R}^n} \left\{ \Phi_p^\mu(\mathbf{x}) + \frac{1}{2\mu} \|\mathbf{x} - \mathbf{a}\|^2 \right\},$$

where $\Phi_p^\mu(\mathbf{x}) := \sum_{i=1}^n \phi_p^\mu(x_i)$ with $\phi_p^\mu(x_i)$ being even, concave, nondecreasing and continuous on $[0, \infty]$, differentiable on $(0, \infty)$, nondifferentiable at 0 with the subdifferential being $\partial \phi_p^\mu(0) = [-1, 1]$. We refer the reader to [51, Theorem 1] (also [53], [56]) for more details. Notice that the p -shrinkage operator is available to matrix variables. Specifically, for the optimization problem

$$\min_X \Phi_p^\mu(X) + \frac{1}{2\mu} \|X - A\|_F^2, \quad (6)$$

we have its globally optimal solution given by

$$X^* = U \mathbf{pshrink}(\Lambda, \mu, p) V^\top, \quad (7)$$

where $A = U \Lambda V^\top$ is the SVD of A and

$$\mathbf{pshrink}(\Lambda, \mu, p) = \mathbf{pshrink}(\sigma(A), \mu, p).$$

III. MODELS AND ALGORITHM

In this section, we aim to develop DCT-based sparse plus nonconvex functions induced low-rank tensor completion approaches to images and videos recovery. Mathematically, we first introduce a unified ‘‘sparse + low-rank’’ tensor completion model for N -th order tensors as follows:

$$\begin{aligned} \min_{\mathcal{X}} \quad & \text{rank}(\mathcal{X}) + \lambda \|\mathcal{D}(\mathcal{X})\|_0 \\ \text{s.t.} \quad & \mathcal{P}_\Omega(\mathcal{X}) = \mathcal{P}_\Omega(\mathcal{H}), \end{aligned} \quad (8)$$

where $\mathcal{D}(\cdot)$ denotes the multi-dimensional DCT operator satisfying orthogonality, $\|\cdot\|_0$ represents the so-called ℓ_0 -norm to characterize the sparsity of DCT’s coefficients, and $\lambda > 0$ is a

tuning parameter. Due to the appearances of rank function and ℓ_0 norm, the optimization model (8) is a highly non-convex and NP-hard problem. Usually, we can find an approximate solution of (8) by employing the (non-) convex relaxations of rank function and ℓ_0 -norm, respectively. Therefore, in this section, we first introduce a DCT-based sparse plus weighted nuclear norm (WNN) induced low-rank tensor completion model. Then, we propose a DCT-based sparse plus p -shrinking mapping induced low-rank tensor completion model. Additionally, we will propose two implementable augmented Lagrangian-based splitting methods to solve the underlying models.

A. DCT-based sparse + WNN induced low-rank minimization model

As shown in the literature, directly minimizing the sum of the rank function and ℓ_0 -norm of tensor \mathcal{X} in (8) is not an easy task. So, how to approximate the rank of tensors is crucial for improving the completion quality. In this subsection, we use the sum of the weighted nuclear norms of the unfolding matrices to approximate the rank of \mathcal{X} and employ the ℓ_1 -norm to replace the ℓ_0 -norm for promoting the sparsity of images under the DCT. Accordingly, we call the model DCT-based sparse + WNN induced low-rank minimization model, which is expressed as the form

$$\begin{aligned} \min_{\mathcal{X}} \quad & \sum_{i=1}^N \alpha_i \|X_{(i)}\|_{*, \mathbf{w}} + \lambda \|\mathcal{D}(\mathcal{X})\|_1 \\ \text{s.t.} \quad & \mathcal{P}_\Omega(\mathcal{X}) = \mathcal{P}_\Omega(\mathcal{H}). \end{aligned} \quad (9)$$

Apparently, two parts of the objective function in model (9) are nonsmooth, but both have promising structures so that their proximal operators enjoy explicit forms. To exploit the structure of model (9), we here first introduce auxiliary variables to separate the two nonsmooth terms in the objective function, thereby leading to a separable optimization model, i.e.,

$$\begin{aligned} \min_{\mathcal{X}} \quad & \sum_{i=1}^N \alpha_i \|Y_{i,(i)}\|_{*, \mathbf{w}} + \lambda \|\mathcal{T}\|_1 \\ \text{s.t.} \quad & \mathcal{X} = \mathcal{Y}_i, \quad \text{for all } i \in [N], \\ & \mathcal{T} = \mathcal{D}(\mathcal{X}), \\ & \mathcal{P}_\Omega(\mathcal{X}) = \mathcal{P}_\Omega(\mathcal{H}). \end{aligned} \quad (10)$$

where $Y_{i,(i)}$ represents the mode- i unfolding of tensor \mathcal{Y}_i for $i \in [N]$. Clearly, model (10) is an equality-constrained optimization problem, then its augmented Lagrangian function reads as

$$\begin{aligned} L(\mathcal{Y}_i, \mathcal{X}, \mathcal{T}, \mathcal{S}_i, \mathcal{Q}) \\ := \sum_{i=1}^N \left(\alpha_i \|Y_{i,(i)}\|_{*, \mathbf{w}} + \langle \mathcal{S}_i, \mathcal{X} - \mathcal{Y}_i \rangle + \frac{\beta}{2} \|\mathcal{X} - \mathcal{Y}_i\|_F^2 \right) \\ + \lambda \|\mathcal{T}\|_1 + \langle \mathcal{Q}, \mathcal{T} - \mathcal{D}(\mathcal{X}) \rangle + \frac{\beta}{2} \|\mathcal{T} - \mathcal{D}(\mathcal{X})\|_F^2, \end{aligned} \quad (11)$$

where \mathcal{S}_i and \mathcal{Q} are Lagrangian multipliers associated to $X_{(i)} = Y_{i,(i)}$ and $\mathcal{T} = \mathcal{D}(\mathcal{X})$, respectively, and β are positive penalty parameters. By (11), we follow the alternating spirit of ADMM to design an implementable algorithm. Theoretically, all primal variables can be updated in any order due to their

equal roles. However, their updating order is slightly sensitive to the numerical performance. Notice that the weight of the low-rank term is usually greater than the sparse part, we empirically first update \mathcal{Y}_i and then calculate \mathcal{X} due to newly introduced equality constraint. Thirdly, we update \mathcal{T} for the reason that we can immediately utilize the latest information of \mathcal{X} . Finally, we update the Lagrangian multipliers \mathcal{S}_i and \mathcal{Q} simultaneously. Therefore, we accordingly update the variables in (11) via the order $\mathcal{Y}_i \rightarrow \mathcal{X} \rightarrow \mathcal{T} \rightarrow \mathcal{S}_i \rightarrow \mathcal{Q}$. Specifically, for given $(\mathcal{X}^k, \mathcal{T}^k, \mathcal{S}_i^k, \mathcal{Q}^k)$, we update the $(k+1)$ -th iterates via the following process:

- The update of \mathcal{Y}_i ($i \in [N]$) reads as

$$\begin{aligned} \mathcal{Y}_i^{k+1} &= \arg \min_{\mathcal{Y}_i} \mathbf{L}(\mathcal{Y}_i, \mathcal{X}^k, \mathcal{T}^k, \mathcal{S}_i^k, \mathcal{Q}^k) \\ &= \arg \min_{\mathcal{Y}_i} \left\{ \alpha_i \|Y_{i,(i)}\|_{*,w} + \frac{\beta_k}{2} \left\| \mathcal{Y}_i - \widehat{\mathcal{Y}}_i^k \right\|_F^2 \right\} \\ &= \text{fold} \left(U_k \mathbf{wshrink} \left(\Lambda^k, \frac{\alpha_i}{\beta_k}, \mathbf{w}_i \right) V_k^\top \right), \end{aligned} \quad (12)$$

where ‘fold(\cdot)’ corresponds to the inverse operator of mode- i unfolding, ‘wshrink(\cdot, \cdot, \cdot)’ is given by (5) and

$$\widehat{\mathcal{Y}}_i^k = \mathcal{X}^k + \frac{1}{\beta_k} \mathcal{S}_i^k \quad \text{and} \quad \widehat{Y}_{i,(i)}^k = U_k \Lambda^k V_k^\top.$$

- With the latest \mathcal{Y}_i^{k+1} , we obtain \mathcal{X}^{k+1} via solving

$$\min_{\mathcal{X}} \left\{ \mathbf{L}(\mathcal{Y}_i^{k+1}, \mathcal{X}, \mathcal{T}^k, \mathcal{S}_i^k, \mathcal{Q}^k) \mid \mathcal{P}_\Omega(\mathcal{X}) = \mathcal{P}_\Omega(\mathcal{H}) \right\},$$

which can be expressed explicitly by

$$\begin{cases} \mathcal{X}_\Omega^{k+1} = \mathcal{H}_\Omega, \\ \mathcal{X}_{\Omega^c}^{k+1} = \frac{1}{N+1} \widehat{\mathcal{X}}_{\Omega^c}^k, \end{cases} \quad (13)$$

where Ω^c denotes the complementary set of Ω and

$$\widehat{\mathcal{X}}^k = \sum_{i=1}^N \left(\mathcal{Y}_i^{k+1} - \frac{1}{\beta_k} \mathcal{S}_i^k \right) + \mathcal{D}^{-1} \left(\mathcal{T}^k + \frac{1}{\beta_k} \mathcal{Q}^k \right).$$

- For the \mathcal{T} -subproblem, we have

$$\begin{aligned} \mathcal{T}^{k+1} &= \arg \min_{\mathcal{T}} \mathbf{L}(\mathcal{Y}_i^{k+1}, \mathcal{X}^{k+1}, \mathcal{T}, \mathcal{S}_i^k, \mathcal{Q}^k) \\ &= \arg \min_{\mathcal{T}} \left\{ \lambda \|\mathcal{T}\|_1 + \frac{\beta_k}{2} \left\| \mathcal{T} - \widehat{\mathcal{T}}^k \right\|_F^2 \right\} \\ &= \text{shrink} \left(\widehat{\mathcal{T}}^k, \frac{\lambda}{\beta_k} \right), \end{aligned} \quad (14)$$

where ‘shrink(\cdot, \cdot)’ is given by (4) and

$$\widehat{\mathcal{T}}^k = \mathcal{D}(\mathcal{X}^{k+1}) - \frac{1}{\beta_k} \mathcal{Q}^k.$$

- With the above latest $(\mathcal{Y}_i^{k+1}, \mathcal{X}^{k+1}, \mathcal{T}^{k+1})$, we update the two Lagrangian multipliers \mathcal{S}_i^{k+1} and \mathcal{Q}^{k+1} via

$$\mathcal{S}_i^{k+1} = \mathcal{S}_i^k + \beta_k (\mathcal{X}^{k+1} - \mathcal{Y}_i^{k+1}) \quad (15)$$

and

$$\mathcal{Q}^{k+1} = \mathcal{Q}^k + \beta_k (\mathcal{T}^{k+1} - \mathcal{D}(\mathcal{X}^{k+1})), \quad (16)$$

respectively.

With the above preparations, we formally summarize the updating schemes for model (10) in Algorithm 1.

Algorithm 1 ADMM for Model (10)

Input: Initial starting points $\mathcal{X}^0, \mathcal{Y}^0, \mathcal{T}^0, \mathcal{S}_0, \mathcal{Q}_0$ and $\beta_0 > 0$.

- 1: Update \mathcal{Y}_i^{k+1} simultaneously via (12) for $i = [N]$;
- 2: Update \mathcal{X}^{k+1} via (13);
- 3: Update \mathcal{T}^{k+1} via (14);
- 4: Update \mathcal{S}_i^{k+1} simultaneously via (15) for $i = [N]$;
- 5: Update \mathcal{Q}^{k+1} via (16);
- 6: Update $\beta_{k+1} = \varrho \beta_k$ with $\varrho > 1$;
- 7: Until a termination criterion is fulfilled.

Output: \mathcal{X}^* .

B. DCT-based sparse + p -shrinking mapping induced low-rank optimization model

In model (9), we employ the sum of the weighted nuclear norms of the unfolding matrices $X_{(i)}$ to approximate the low-rankness of the data. However, we do not know whether such an approximation is enough ideal for color images and videos tensor data. Recently, the so-called p -shrinking algorithm is widely used in low-rank and sparse recovery problems. Hence, in this subsection, we further consider the combination of p -shrinking low-rank penalty and DCT-driven sparse regularization, and propose the following tensor completion model:

$$\begin{aligned} \min_{\mathcal{X}} \quad & \sum_{i=1}^N \alpha_i \Phi_p^u(X_{(i)}) + \lambda \|\mathcal{D}(\mathcal{X})\|_1 \\ \text{s.t.} \quad & \mathcal{P}_\Omega(\mathcal{X}) = \mathcal{P}_\Omega(\mathcal{H}), \end{aligned} \quad (17)$$

where $p \leq 1$ and $\Phi_p^u(\cdot)$ is a nonconvex penalty function defined in (6). Compared to model (9), the only difference is that we here employ the $\Phi_p^u(X_{(i)})$ to replace the weighted nuclear norm term $\|X_{(i)}\|_{*,w}$. So, both (9) and (17) share the same structure except the low-rank-inducing term. For simplicity, we use the symbols in (10) again, then model (17) can be rewritten as the following separable optimization problem, i.e.,

$$\begin{aligned} \min_{\mathcal{X}} \quad & \sum_{i=1}^N \alpha_i \Phi_p^u(Y_{i,(i)}) + \lambda \|\mathcal{T}\|_1 \\ \text{s.t.} \quad & \mathcal{X} = \mathcal{Y}_i, \quad \text{for all } i \in [N], \\ & \mathcal{T} = \mathcal{D}(\mathcal{X}), \\ & \mathcal{P}_\Omega(\mathcal{X}) = \mathcal{P}_\Omega(\mathcal{H}). \end{aligned} \quad (18)$$

Correspondingly, the augmented Lagrangian function for (18) reads as

$$\begin{aligned} & \mathbf{L}(\mathcal{Y}_i, \mathcal{X}, \mathcal{T}, \mathcal{S}_i, \mathcal{Q}) \\ & := \sum_{i=1}^N \left(\alpha_i \Phi_p^u(Y_{i,(i)}) + \langle \mathcal{S}_i, \mathcal{X} - \mathcal{Y}_i \rangle + \frac{\beta}{2} \|\mathcal{X} - \mathcal{Y}_i\|_F^2 \right) \\ & \quad + \lambda \|\mathcal{T}\|_1 + \langle \mathcal{Q}, \mathcal{T} - \mathcal{D}(\mathcal{X}) \rangle + \frac{\beta}{2} \|\mathcal{T} - \mathcal{D}(\mathcal{X})\|_F^2. \end{aligned} \quad (19)$$

Based upon (19), by invoking the update idea of Algorithm 1, i.e., $\mathcal{Y}_i \rightarrow \mathcal{X} \rightarrow \mathcal{T} \rightarrow \mathcal{S}_i \rightarrow \mathcal{Q}$, we derive the detailed iterative schemes for solving model (18).

- Update \mathcal{Y}_i^{k+1} via

$$\begin{aligned} \mathcal{Y}_i^{k+1} &= \arg \min_{\mathcal{Y}_i} \mathbf{L}(\mathcal{Y}_i, \mathcal{X}^k, \mathcal{T}^k, \mathcal{S}_i^k, \mathcal{Q}^k) \\ &= \arg \min_{\mathcal{Y}_i} \left\{ \alpha_i \Phi_p^\mu(Y_{i,(i)}) + \frac{\beta_k}{2} \left\| \mathcal{Y}_i - \widehat{\mathcal{Y}}_i^k \right\|_F^2 \right\} \\ &= \text{fold} \left(\widetilde{U}_k \text{pshrink} \left(\widetilde{\Lambda}^k, \frac{\alpha_i}{\beta_k}, p \right) \widetilde{V}_k^\top \right), \quad (20) \end{aligned}$$

where ‘pshrink(\cdot, \cdot, \cdot)’ is given by (3) and

$$\widehat{\mathcal{Y}}_i^k = \mathcal{X}^k + \frac{1}{\beta_k} \mathcal{S}_i^k \quad \text{and} \quad \widehat{Y}_{i,(i)}^k = \widetilde{U}_k \widetilde{\Lambda}^k \widetilde{V}_k^\top.$$

- We obtain \mathcal{X}^{k+1} via solving

$$\min_{\mathcal{X}} \{ \mathbf{L}(\mathcal{Y}_i^{k+1}, \mathcal{X}, \mathcal{T}^k, \mathcal{S}_i^k, \mathcal{Q}^k) \mid \mathcal{P}_\Omega(\mathcal{X}) = \mathcal{P}_\Omega(\mathcal{H}) \},$$

which can also be expressed explicitly by

$$\begin{cases} \mathcal{X}_\Omega^{k+1} = \mathcal{H}_\Omega, \\ \mathcal{X}_{\Omega^c}^{k+1} = \frac{1}{N+1} \widehat{\mathcal{X}}_\Omega^k \end{cases} \quad (21)$$

where

$$\widehat{\mathcal{X}}^k = \sum_{i=1}^N \left(\mathcal{Y}_i^{k+1} - \frac{1}{\beta_k} \mathcal{S}_i^k \right) + \mathcal{D}^{-1} \left(\mathcal{T}^k + \frac{1}{\beta_k} \mathcal{Q}^k \right).$$

- Update \mathcal{T}^{k+1} via

$$\begin{aligned} \mathcal{T}^{k+1} &= \arg \min_{\mathcal{T}} \mathbf{L}(\mathcal{Y}_i^{k+1}, \mathcal{X}^{k+1}, \mathcal{T}, \mathcal{S}_i^k, \mathcal{Q}^k) \\ &= \text{shrink} \left(\mathcal{D}(\mathcal{X}^{k+1}) - \frac{1}{\beta_k} \mathcal{Q}^k, \frac{\lambda}{\beta_k} \right). \quad (22) \end{aligned}$$

- Finally, update the two Lagrangian multipliers \mathcal{S}_i^{k+1} and \mathcal{Q}^{k+1} via (15) and (16), respectively.

Formally, we summarize the iterative schemes for (18) in Algorithm 2.

Algorithm 2 ADMM for Model (18).

Input: Initial starting points $\mathcal{X}^0, \mathcal{Y}^0, \mathcal{T}^0, \mathcal{S}_0, \mathcal{Q}_0$.

- 1: Update \mathcal{Y}_i^{k+1} simultaneously via (20) for $i = [N]$;
- 2: Update \mathcal{X}^{k+1} via (21);
- 3: Update \mathcal{T}^{k+1} via (22);
- 4: Update \mathcal{S}_i^{k+1} simultaneously via (15) for $i = [N]$;
- 5: Update \mathcal{Q}^{k+1} via (16);
- 6: Update $\beta_{k+1} = \varrho \beta_k, \varrho > 1$;
- 7: Until a termination criterion is fulfilled.

Output: \mathcal{X}^* .

C. Convergence results

In this subsection, we follow the way used in [57] to prove the convergence result of Algorithm 1 for problem (10) under some assumptions. Since Algorithm 2 share the almost same iterative schemes except the \mathcal{Y} -subproblem, we skip the convergence analysis of Algorithm 2 for model (18) for the conciseness of the paper.

Lemma 3.1. *Suppose that both $\{\mathcal{S}^k\} := \{\mathcal{S}_1^k, \dots, \mathcal{S}_N^k\}$ and $\{\mathcal{Q}^k\}$ are bounded, the sequences $\{\mathcal{Y}^k\} := \{\mathcal{Y}_1^k, \dots, \mathcal{Y}_N^k\}$ and $\{\mathcal{T}^k\}$ produced by Algorithm 1 are bounded.*

Proof. From the definition of $\mathbf{L}(\mathcal{Y}, \mathcal{X}, \mathcal{T}, \mathcal{S}, \mathcal{Q})$, we have

$$\begin{aligned} &\mathbf{L}(\mathcal{Y}^k, \mathcal{X}^k, \mathcal{T}^k, \mathcal{S}^k, \mathcal{Q}^k) - \mathbf{L}(\mathcal{Y}^k, \mathcal{X}^k, \mathcal{T}^k, \mathcal{S}^{k-1}, \mathcal{Q}^{k-1}) \\ &= \sum_{i=1}^N \langle \mathcal{S}_i^k - \mathcal{S}_i^{k-1}, \mathcal{X}^k - \mathcal{Y}_i^k \rangle + \langle \mathcal{Q}^k - \mathcal{Q}^{k-1}, \mathcal{T}^k - \mathcal{D}(\mathcal{X}^k) \rangle \\ &\quad + \frac{\beta_k - \beta_{k-1}}{2} \left(\sum_{i=1}^N \|\mathcal{X}^k - \mathcal{Y}_i^k\|_F^2 + \|\mathcal{T}^k - \mathcal{D}(\mathcal{X}^k)\|_F^2 \right) \\ &= \frac{1}{\beta_{k-1}} \left(\sum_{i=1}^N \|\mathcal{S}_i^k - \mathcal{S}_i^{k-1}\|_F^2 + \|\mathcal{Q}^k - \mathcal{Q}^{k-1}\|_F^2 \right) \\ &\quad + \frac{\beta_k - \beta_{k-1}}{2\beta_{k-1}^2} \left(\sum_{i=1}^N \|\mathcal{S}_i^k - \mathcal{S}_i^{k-1}\|_F + \|\mathcal{Q}^k - \mathcal{Q}^{k-1}\|_F \right) \\ &= \frac{\beta_k + \beta_{k-1}}{2\beta_{k-1}^2} \left(\sum_{i=1}^N \|\mathcal{S}_i^k - \mathcal{S}_i^{k-1}\|_F^2 + \|\mathcal{Q}^k - \mathcal{Q}^{k-1}\|_F^2 \right), \quad (23) \end{aligned}$$

where the second equality follows from (15) and (16). Then, it follows from the iterative schemes of Algorithm 1 and (23) that

$$\begin{aligned} &\mathbf{L}(\mathcal{Y}^{k+1}, \mathcal{X}^{k+1}, \mathcal{T}^{k+1}, \mathcal{S}^k, \mathcal{Q}^k) \\ &\leq \mathbf{L}(\mathcal{Y}^k, \mathcal{X}^k, \mathcal{T}^k, \mathcal{S}^k, \mathcal{Q}^k) \\ &= \mathbf{L}(\mathcal{Y}^k, \mathcal{X}^k, \mathcal{T}^k, \mathcal{S}^{k-1}, \mathcal{Q}^{k-1}) \\ &\quad + \frac{\beta_k + \beta_{k-1}}{2\beta_{k-1}^2} \left(\sum_{i=1}^N \|\mathcal{S}_i^k - \mathcal{S}_i^{k-1}\|_F^2 + \|\mathcal{Q}^k - \mathcal{Q}^{k-1}\|_F^2 \right). \quad (24) \end{aligned}$$

By invoking $\beta_k = \varrho \beta_{k-1}$ with $\varrho > 1$, we immediately prove $\sum_{i=1}^\infty \frac{\beta_k + \beta_{k-1}}{2\beta_{k-1}^2} < \infty$. As a consequence of (24), the sequence $\{\mathbf{L}(\mathcal{Y}^k, \mathcal{X}^k, \mathcal{T}^k, \mathcal{S}^k, \mathcal{Q}^k)\}$ is upper-bounded due to the boundedness of $\{\mathcal{S}^k\}$ and $\{\mathcal{Q}^k\}$. Rearranging terms of $\{\mathbf{L}(\mathcal{Y}^k, \mathcal{X}^k, \mathcal{T}^k, \mathcal{S}^k, \mathcal{Q}^k)\}$ immediately yields

$$\begin{aligned} &\sum_{i=1}^N \left(\alpha_i \|Y_{i,(i)}^k\|_{*,w} \right) + \lambda \|\mathcal{T}^k\|_1 \\ &= \mathbf{L}(\mathcal{Y}^k, \mathcal{X}^k, \mathcal{T}^k, \mathcal{S}^{k-1}, \mathcal{Q}^{k-1}) - \frac{\beta_{k-1}}{2} (\|\mathcal{Q}^k\|_F^2 - \|\mathcal{Q}^{k-1}\|_F^2) \\ &\quad - \frac{\beta_{k-1}}{2} \sum_{i=1}^N (\|\mathcal{S}_i^k\|_F^2 - \|\mathcal{S}_i^{k-1}\|_F^2), \end{aligned}$$

which, together with the boundedness of the sequences $\{\mathbf{L}(\mathcal{Y}^k, \mathcal{X}^k, \mathcal{T}^k, \mathcal{S}^{k-1}, \mathcal{Q}^{k-1})\}$, $\{\mathcal{S}^k\}$ and $\{\mathcal{Q}^k\}$, implies that $\{Y_{i,(i)}^k\}$ and $\{\mathcal{T}^k\}$ for all $i \in [N]$ are bounded, since $\|\cdot\|_{*,w}$ and $\|\cdot\|_1$ are nonnegative. \square

Theorem 3.2. *Let $\{\mathcal{Y}^k, \mathcal{X}^k, \mathcal{T}^k, \mathcal{S}^k, \mathcal{Q}^k\}$ be a sequence generated by Algorithm 1. Suppose that both $\{\mathcal{S}^k\}$ and $\{\mathcal{Q}^k\}$ are bounded, and further satisfy $\lim_{k \rightarrow \infty} \|\mathcal{S}^{k+1} - \mathcal{S}^k\|_F = 0$ and $\lim_{k \rightarrow \infty} \|\mathcal{Q}^{k+1} - \mathcal{Q}^k\|_F = 0$, respectively. Then,*

- (i). $\{\mathcal{X}^k\}, \{\mathcal{Y}^k\}, \{\mathcal{T}^k\}$ are bounded Cauchy sequences.
- (ii). any accumulation point $\{(\mathcal{Y}^\infty, \mathcal{X}^\infty, \mathcal{T}^\infty, \mathcal{S}^\infty, \mathcal{Q}^\infty)\}$ satisfies the KKT condition of model (10).

Proof. For any $i \in [N]$, it easily follows from the iterative scheme (15) and $\lim_{k \rightarrow \infty} \beta_k = \infty$ that the sequence $\{\mathcal{X}^k\}$ is bounded due to Lemma 3.1. Moreover, by the properties of $\{\mathcal{S}^k\}$ and $\{\mathcal{Q}^k\}$, we have

$$\begin{cases} \lim_{k \rightarrow \infty} \|\mathcal{X}^{k+1} - \mathcal{Y}_i^{k+1}\|_F = 0, \\ \lim_{k \rightarrow \infty} \|\mathcal{T}^{k+1} - \mathcal{D}(\mathcal{X}^{k+1})\|_F = 0, \end{cases} \quad (25)$$

which further implies that $\{\mathcal{Y}^k\}$ and $\{\mathcal{T}^k\}$ approach to feasible solutions.

Now, we show that $\{\mathcal{X}^k\}$, $\{\mathcal{Y}^k\}$, $\{\mathcal{T}^k\}$ are Cauchy sequences. Here, we only show $\{\mathcal{Y}^k\}$ being a Cauchy sequence, while the other sequences can be proved in a similar way.

Invoking the first-order optimality condition of the \mathcal{Y} -subproblem yields

$$0 \in \alpha_i \partial_C \|Y_{i,(i)}^{k+1}\|_{*,w} - \beta_k \left(X_{(i)}^k - Y_{i,(i)}^{k+1} + \frac{1}{\beta_k} S_{i,(i)}^k \right),$$

which, together with (15), leads to

$$X_{(i)}^k - X_{(i)}^{k+1} \in \frac{\alpha_i \partial_C \|Y_{i,(i)}^{k+1}\|_{*,w} - S_{i,(i)}^{k+1}}{\beta_k}. \quad (26)$$

By the boundedness of both $\{Y_{i,(i)}^k\}$ and $\{S_{i,(i)}^k\}$ and properties of $\|\cdot\|_{*,w}$, it follows from (26) that $\|X_{(i)}^k - X_{(i)}^{k+1}\|_F = O(\beta_k^{-1})$, which together with $\sum_{i=0}^{\infty} \beta_k^{-1} = \frac{\rho}{\beta_0(\rho-1)} < \infty$, implies that $\{X^k\}$ is a Cauchy sequence, and it immediately has a limit point.

Let \mathcal{X}^∞ , \mathcal{Y}^∞ , \mathcal{T}^∞ , \mathcal{S}^∞ , \mathcal{Q}^∞ be the limit points of $\{X^k\}$, $\{Y^k\}$, $\{T^k\}$, $\{S^k\}$, $\{Q^k\}$, respectively. It first follows from (25) that

$$\mathcal{X}^\infty = \mathcal{Y}_i^\infty, (i = 1, \dots, N) \text{ and } \mathcal{T}^\infty = \mathcal{D}(\mathcal{X}^\infty).$$

Rearranging (26) arrives at

$$\begin{aligned} 0 &\in \alpha_i \partial_C \|Y_{i,(i)}^{k+1}\|_{*,w} - S_{i,(i)}^{k+1} - \beta_k \left(X_{(i)}^k - X_{(i)}^{k+1} \right) \\ &= \alpha_i \partial_C \|Y_{i,(i)}^{k+1}\|_{*,w} - S_{i,(i)}^{k+1} - \beta_k \left(X^k - X^{k+1} \right). \end{aligned} \quad (27)$$

Consequently, taking limit on (27) immediately yields $\mathcal{S}_i^\infty \in \alpha_i \partial_C \|\mathcal{Y}_i^\infty\|_{*,w}$.

By the first-order optimality condition of the \mathcal{X} -subproblem, we have \bar{X}

$$\begin{cases} \sum_{i=1}^N (S_i^k + \beta_k (\mathcal{X}^{k+1} - \mathcal{Y}_i^{k+1})) \\ + \beta_k (\mathcal{X}^{k+1} - \mathcal{D}^{-1}(\mathcal{T}^k)) - \mathcal{D}^{-1}(\mathcal{Q}^k) = 0, \\ \mathcal{P}_\Omega(\mathcal{X}^{k+1}) = \mathcal{P}_\Omega(\mathcal{H}), \end{cases}$$

Taking $k \rightarrow \infty$ on the above two equalities leads to

$$\sum_{i=1}^N \mathcal{S}_i^\infty = \mathcal{D}^{-1}(\mathcal{Q}^\infty) \text{ and } \mathcal{P}_\Omega(\mathcal{X}^\infty) = \mathcal{P}_\Omega(\mathcal{H}).$$

Finally, the first-order optimality condition of the \mathcal{T} -subproblem reads as

$$\begin{aligned} 0 &\in \partial \lambda \|\mathcal{T}^{k+1}\|_1 + \beta_k (\mathcal{T}^{k+1} - \mathcal{D}(X^{k+1}) + \beta_k^{-1} \mathcal{Q}^k) \\ &= \partial \lambda \|\mathcal{T}^{k+1}\|_1 + \mathcal{Q}^k + \beta_k (\mathcal{T}^{k+1} - \mathcal{D}(\mathcal{X}^{k+1})) \\ &= \partial \lambda \|\mathcal{T}^{k+1}\|_1 + \mathcal{Q}^{k+1}. \end{aligned}$$

Consequently, we have $-\mathcal{Q}^* \in \partial \lambda \|\mathcal{T}^*\|_1$ when $k \rightarrow \infty$.

Therefore, we conclude that the accumulation point satisfies the KKT condition of model (10). \square

Hereafter, we only give the time complexity analysis of Algorithm 1 and omit the analysis of Algorithm 2 since both of them share the almost iterative scheme and the same SVD.

The main time cost of Algorithm 1 is consuming by performing SVD and multi-dimensional DCT. In each iteration, the complexity of subproblem \mathcal{Y}_i^{k+1} ($i \in [N]$) is $O\left(\sum_{i=1}^N (I_i)^2 \times \prod_{j \neq i} I_j\right)$. The complexities of subproblem \mathcal{X}^{k+1} and \mathcal{T}^{k+1} are both $O\left(\prod_{i=1}^N I_i \times \log \prod_{i=1}^N I_i\right)$. In addition, the complexities to update \mathcal{S}_i^{k+1} ($i \in [N]$) and \mathcal{Q}^{k+1} are $O(N \prod_{i=1}^N I_i)$ and $O(\prod_{i=1}^N I_i)$. So, the time complexity of each iteration is $O\left(\sum_{i=1}^N (I_i)^2 \times \prod_{j \neq i} I_j + \prod_{i=1}^N I_i \times \log \prod_{i=1}^N I_i\right)$. Thus, the total time complexity of Algorithm 1 is $O\left(t \left(\sum_{i=1}^N (I_i)^2 \times \prod_{j \neq i} I_j + \prod_{i=1}^N I_i \times \log \prod_{i=1}^N I_i\right)\right)$, where t is the number of iterations.

IV. NUMERICAL EXPERIMENTS

In this section, we are concerned with the numerical performance of our approach proposed in Section III on images and videos recovery. Here, we will consider two kinds of images and videos data sets: 1) RGB images; 2) surveillance videos. All algorithms were implemented in MATLAB R2018b (64bit) and experiments were conducted on a laptop computer with Intel(R) Core(TM) i7-7500 CPU @2.70GHz and 8GB memory. Throughout this section, we denote Algorithms 1 and 2 by ‘DCT-WNN’ and ‘DCT-IpST’ for simplicity, respectively. Moreover, we also compare the proposed algorithms with eight state-of-the-art tensor completion approaches as follows:

- IpST [53]: Iterative p -shrinkage thresholding algorithm for solving low Tucker rank tensor recovery problem, which only employs a nonconvex penalty function $\Phi_p^\mu(\cdot)$ given in (6) to replace the traditional nuclear norm of unfolding matrices.
- TTNNL1 [44]: Using the truncated tensor nuclear norm for low-rank approximation, and a sparse regularization term combined with the 3-D DCT bases.
- F-TNN [48]¹: Framelet representation of tensor nuclear norm for third-order tensor completion.
- TNN-3DTV [39]: Anisotropic total variation regularized low-rank tensor completion based on tensor nuclear norm, which utilizes the 3D total variation regularization to exploit the structure of images.
- TCTF [12]²: Tensor factorization for low-rank tensor completion, which uses the operation of T-product to decompose a tensor into two smaller tensors.
- WSTNN [58]³: Tensor N-tubal rank and its convex relaxation for low-rank tensor recovery, which defines the weighted sum of the tensor nuclear norm.
- SMF-LRTC [59]⁴: Low-rank tensor completion via smooth matrix factorization, which exploits the piecewise

¹<https://github.com/TaiXiangJiang/Framelet-TNN>

²<https://panzhous.github.io/>

³<https://yubangzheng.github.io/ybz/>

⁴<https://github.com/zhaoxile/Low-rank-tensor-completion-via-smooth-matrix-factorization>

smoothness prior of tensors by introducing smoothness constraints on the factor matrices. Here, we only use it for video experiments, because such a model is designed for video and hyperspectral image data sets.

- DP3LRTC [50]: Using tensor nuclear norm to characterize the global low-rankness prior and plugging a denoising neural network, which learned from a large number of natural images. It is a deep learning method.

For the fair comparison, we take

$$\text{RelCha} = \frac{\|\mathcal{X}^{k+1} - \mathcal{X}^k\|_F}{\|\mathcal{X}_{\text{true}}\|_F} \leq 10^{-4}, \quad (28)$$

as the stopping criterion for all methods, where $\mathcal{X}_{\text{true}}$ is the true tensor. Moreover, the following metrics are chosen to evaluate the recovery performance of the different algorithms.

- Peak Signal-to-Noise Ratio (PSNR [12]) is defined as:

$$\text{PSNR} = 10 \log_{10} \frac{(\#\mathcal{X}_{\text{true}}) \cdot (\mathcal{X}_{\text{true}}^{\max})^2}{\|\mathcal{X}^* - \mathcal{X}_{\text{true}}\|_F^2}$$

to measure the quality of the restored tensor data by an algorithm, where $(\#\mathcal{X}_{\text{true}})$ denotes the number of elements of $\mathcal{X}_{\text{true}}$, $\mathcal{X}_{\text{true}}^{\max}$ represents the largest element of $\mathcal{X}_{\text{true}}$, and \mathcal{X}^* corresponds to the restored tensor.

- Structural Similarity (SSIM [60])⁵ is defined as:

$$\text{SSIM} = \frac{(2\mu_X\mu_{X^*} + a_1)(2\sigma_{XX^*} + a_2)}{(\mu_X^2 + \mu_{X^*}^2 + a_1)(\sigma_X^2 + \sigma_{X^*}^2 + a_2)},$$

where X and X^* denote the greyscale images for the original image and its recovered image, respectively; a_1 and a_2 are constants; μ_X and μ_{X^*} denote the average values, while σ_X and σ_{X^*} denote the standard deviation of X and X^* , respectively; and σ_{XX^*} denote the covariance matrix between X and X^* .

Since there are some parameters in models and algorithms, for both models (10) and (18), we set $(\alpha_1, \alpha_2, \alpha_3) = (1/3, 1/3, 10^{-3})$ for image inpainting and $(\alpha_1, \alpha_2, \alpha_3) = (1/3, 1/3, 1/3)$ for video inpainting, respectively. Moreover, we take $\lambda = 0.05$ and $\lambda = 10^{-2}$ for (10) and (18), respectively. For the algorithmic parameters, we set $p = 0.2$ for DCT-IpST throughout the experiments. In addition, we set $\varrho = 1.2$ and $\beta^0 = 10^{-5}$, respectively. All parameters of the other compared algorithms were taken as the default values used in the paper.

A. RGB image inpainting

In this subsection, we consider the RGB image inpainting problem, where RGB images namely include Red, Green, and Blue channels and the number of channels corresponds to the modes of a third order tensor. Here, we conduct the numerical performance our approach on 16 widely used images⁶, which are summarized in Fig. 2. Here, the eight images in the first two rows of Fig. 2 are $256 \times 256 \times 3$, and the remaining eight images are $512 \times 768 \times 3$ except image **woman** of size $768 \times 512 \times 3$. These images have no visual features such as low-rank and sparsity. However, as shown in Fig. 3, the sparse structure is apparent when applying DCT to these

images, which also sufficiently supports that the main idea of this paper is reasonable.



Fig. 2. The sixteen RGB images for experiments.

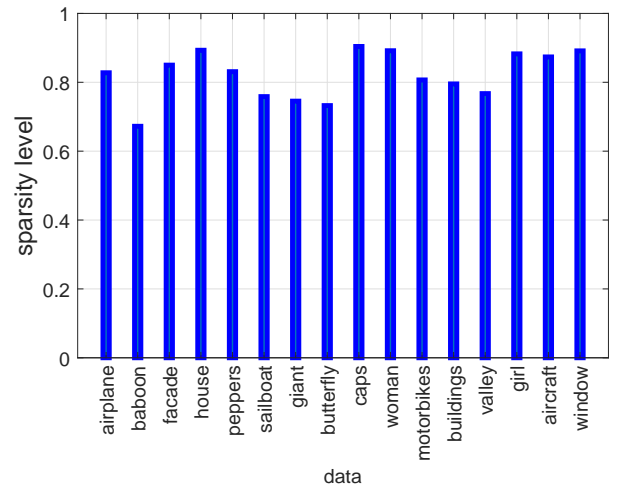


Fig. 3. Sparsity level of sixteen RGB images under DCT, where “sparsity level” is defined as the proportion of the number of zero elements in a tensor.

Now, we are concerned with the inpainting performance of our approach on the cases where the pixels of images are missed in a random way. In Fig. 4, we first consider four scenarios on the sampling rate (‘sr’), i.e., $\text{sr} = \{3\%, 5\%, 10\%, 20\%\}$, for five images. Clearly, except the deep learning method DP3LRTC, the recovered images by our methods, i.e., DCT-WNN and DCT-IpST, are better than the other compared model-driven methods for the scenarios where sr’s are lower than 10% (see the first four columns of Fig. 4). To investigate the full sensitivity of these methods to sr, we further consider five scenarios on sr’s from 3% to 30% for the images listed in Fig. 2, and plot PSNR values with respect to

⁵MATLAB package: <https://ece.uwaterloo.ca/~z70wang/research/ssim/>.

⁶<http://r0k.us/graphics/kodak/>

sr's in Fig. 5. It can be easily seen from Fig. 5 that both DCT-WNN and DCT-IpST outperform the other compared methods except the deep learning method DP3LRTC in terms of taking higher PSNR values for all scenarios with $sr \leq 20\%$.

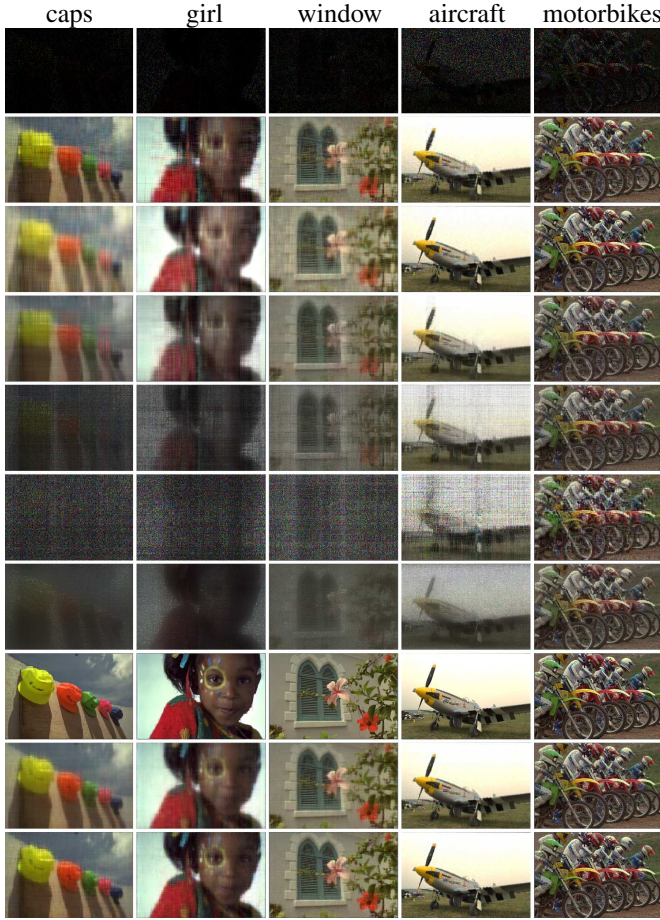


Fig. 4. Images recovered by the nine algorithms for the cases with random missing information. The top row corresponds to the observed incomplete images. From left to right: downsampled images with $sr = 3\%$, 3% , 5% , 10% and 20% , respectively. From the second row to bottom: Images recovered by IpST, TTNNL1, F-TNN, TNN-3DTV, TCTF, WSTNN, DP3LRTC, DCT-IpST and DCT-WNN, respectively.

Below, we are interested in the numerical performance on structurally missing scenarios such as missing slices or shape/text mask (i.e., downsampling operator). Specifically, we consider five scenarios as shown by the first row of Fig. 6. Obviously, we see from the last two rows in Fig. 6 that our DCT-WNN and DCT-IpST have promising ability to recover the structurally missing images. Moreover, from the PSNR, SSIM, and computing time in seconds (TIME(s) for short) reported in Table I, we can see that the proposed DCT-WNN and DCT-IpST have better numerical performance than the compared methods except the deep learning method DP3LRTC. However, our DCT-WNN and DCT-IpST take less computing time than DP3LRTC to achieve comparable PSNR and SSIM values when all methods ran on a general personal computer without GPU acceleration. Those results efficiently demonstrate that the popular deep learning methods usually obtain better inpainting quality than the traditional model-driven approaches. However, model-driven approaches are still

necessary for real-world applications due to their relatively low requirements on computer hardware.

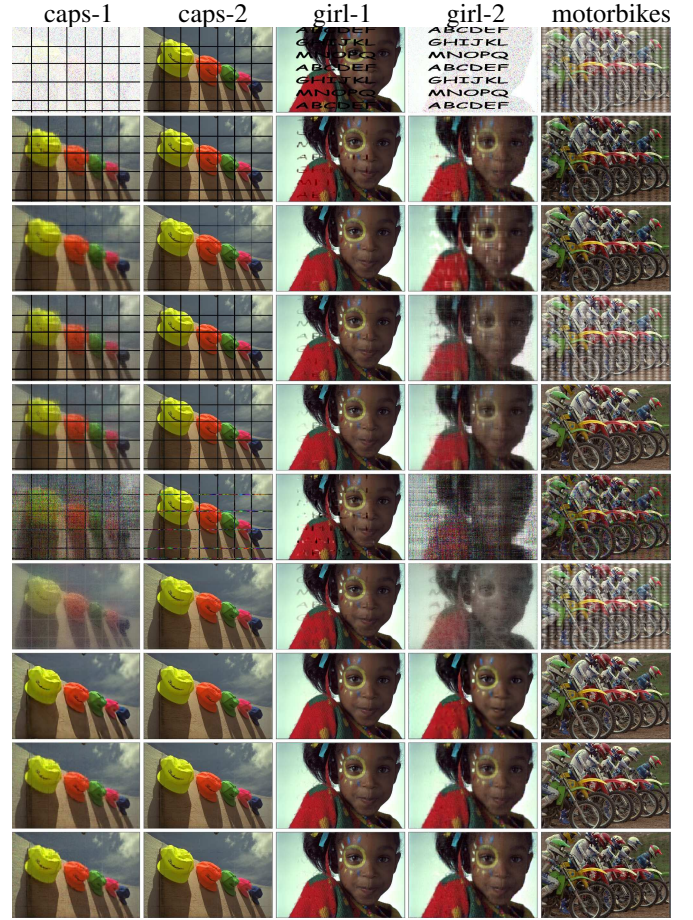


Fig. 6. Images recovered by the nine algorithms for the cases with structurally missing information. From the second row to bottom: Images recovered by IpST, TTNNL1, F-TNN, TNN-3DTV, TCTF, WSTNN, DP3LRTC, DCT-IpST and DCT-WNN, respectively.

B. Video recovery

The above color images are actually low-dimensional third-order tensors. In this subsection, we consider higher dimensional cases, i.e., surveillance video data sets, which are natural third-order and fourth-order tensors corresponding to grayscale and color videos, respectively. Here, we choose six grayscale videos including ‘airport’, ‘sidewalk’⁷, ‘lunges’, ‘biking’, ‘baby’⁸ and ‘basketball’⁹ for experiments. Here, we add a ‘camera-shake’ operation to ‘airport’ and ‘sidewalk’ so that their backgrounds are not static. Typical frames in these videos are depicted in Fig. 7.

We also first check the sparsity level of videos data sets when applying DCT to videos. The results in Fig. 8 clearly demonstrate that videos also appear sparse structure under DCT, since the six video data sets have more than 60% zeros,

⁷<https://gr.xjtu.edu.cn/web/dymeng/3>; the data can also be downloaded from: http://perception.i2r.a-star.edu.sg/bk_model/bk_index.html.

⁸<http://crev.ucf.edu/data/UCF101.php>

⁹<https://github.com/csyongdu/>

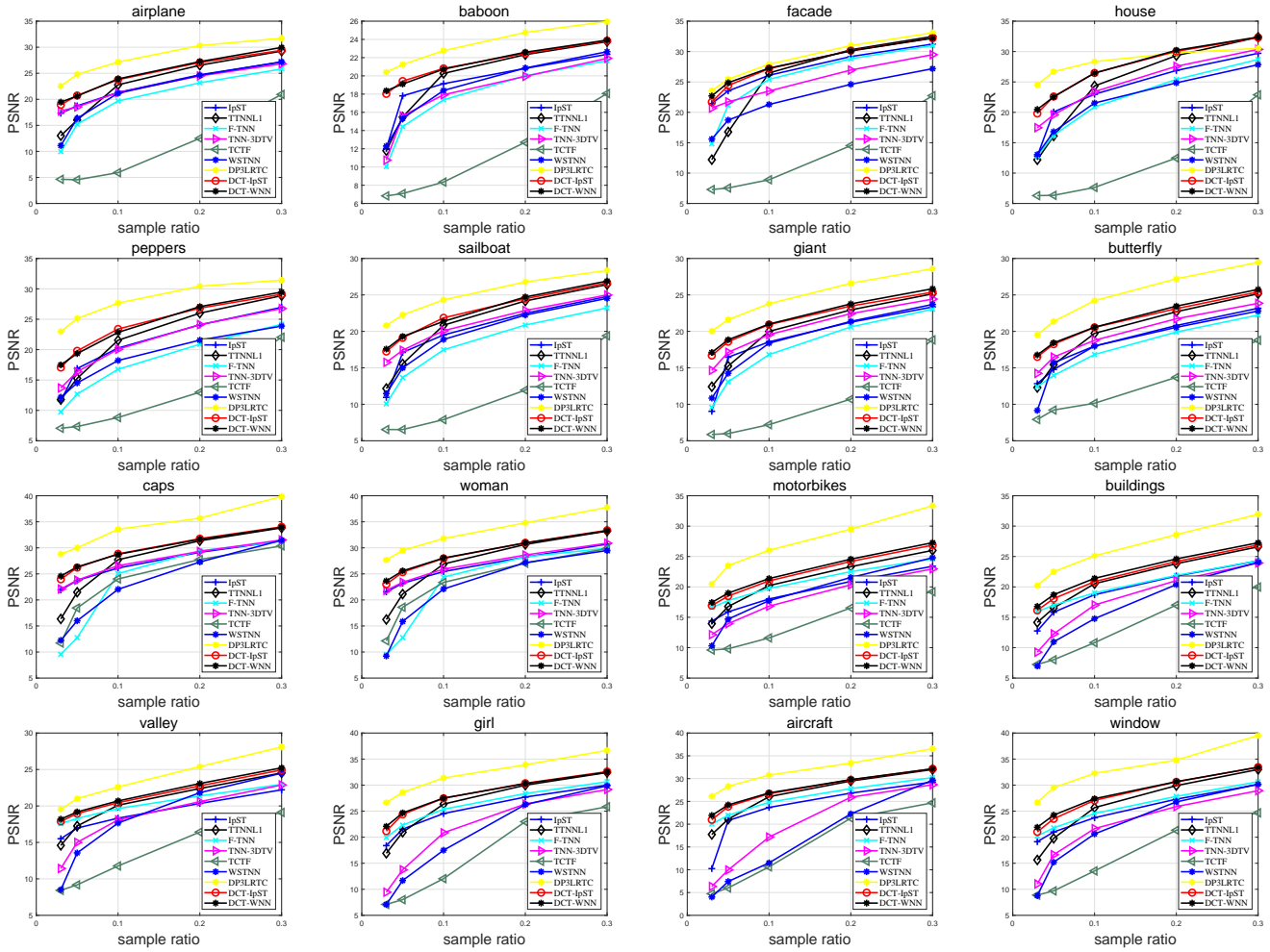


Fig. 5. PSNR values with respect to different sampling rates for the sixteen RGB images in Fig. 2.

TABLE I
NUMERICAL RESULTS OF THE NINE ALGORITHMS FOR RECOVERING IMAGES WITH STRUCTURALLY MISSING PIXELS AS TESTED IN FIG. 6.

Method	caps-1			caps-2			girl-1			girl-2			motorbikes		
	PSNR	SSIM	TIME	PSNR	SSIM	TIME	PSNR	SSIM	TIME	PSNR	SSIM	TIME	PSNR	SSIM	TIME
IpST	17.28	0.558	53.81	17.87	0.749	52.21	25.01	0.892	55.29	23.24	0.668	62.14	16.01	0.902	29.03
TTNNL1	24.07	0.711	55.37	26.86	0.857	55.31	31.22	0.942	53.25	23.70	0.724	56.93	21.62	0.967	46.87
F-TNN	17.00	0.540	135.08	17.87	0.749	25.13	27.61	0.916	97.64	19.11	0.559	137.30	9.80	0.861	34.80
TNN-3DTV	18.96	0.602	315.42	20.47	0.800	300.23	29.38	0.934	361.91	22.47	0.712	323.01	31.96	0.990	322.12
TCTF	12.70	0.130	26.43	18.22	0.753	30.23	25.59	0.863	28.62	10.94	0.135	29.64	16.29	0.742	25.92
WSTNN	19.27	0.639	167.36	34.41	0.965	154.31	29.05	0.881	157.83	16.34	0.576	168.18	10.74	0.884	165.36
DP3LRTC	29.04	0.933	190.79	39.25	0.922	218.53	33.93	0.899	188.16	27.30	0.890	183.15	35.90	0.987	182.67
DCT-IpST	28.08	0.842	102.59	35.84	0.973	100.13	31.79	0.946	99.67	26.10	0.821	101.77	32.90	0.991	100.06
DCT-WNN	28.15	0.831	116.81	36.09	0.974	102.33	31.76	0.943	100.07	26.22	0.807	114.25	23.85	0.975	101.55

which means that DCT is an ideal technique for promoting sparsity of video data sets.

Now, we turn our attention to investigating the performance of our approach on incomplete videos data. In our experiments, we conduct four scenarios on the sampling rate, i.e., $sr = \{5\%, 10\%, 20\%, 30\%\}$, for the six video data sets. The PSNR, SSIM and TIME(s) values of the six videos obtained by the algorithms are summarized in Table II, which shows that both DCT-IpST and DCT-WNN perform better than the other compared methods except the deep learning method DP3LRTC

for the low sampling rate cases (i.e., $sr \leq 20\%$). Here, it is noteworthy that the deep learning method DP3LRTC does not necessarily always achieve the best results. For example, our approach either DCT-WNN or DCT-IpST works better than DP3LRTC for “basketball” and “luniges” in some cases. More interestingly, our DCT-WNN and DCT-IpST always take much less computing time than DP3LRTC for video data sets to achieve comparable inpainting quality. In Fig. 9, we first display the destroyed (downsampled) frames (ten consecutive frames) are listed in the first row, and the recovered frames

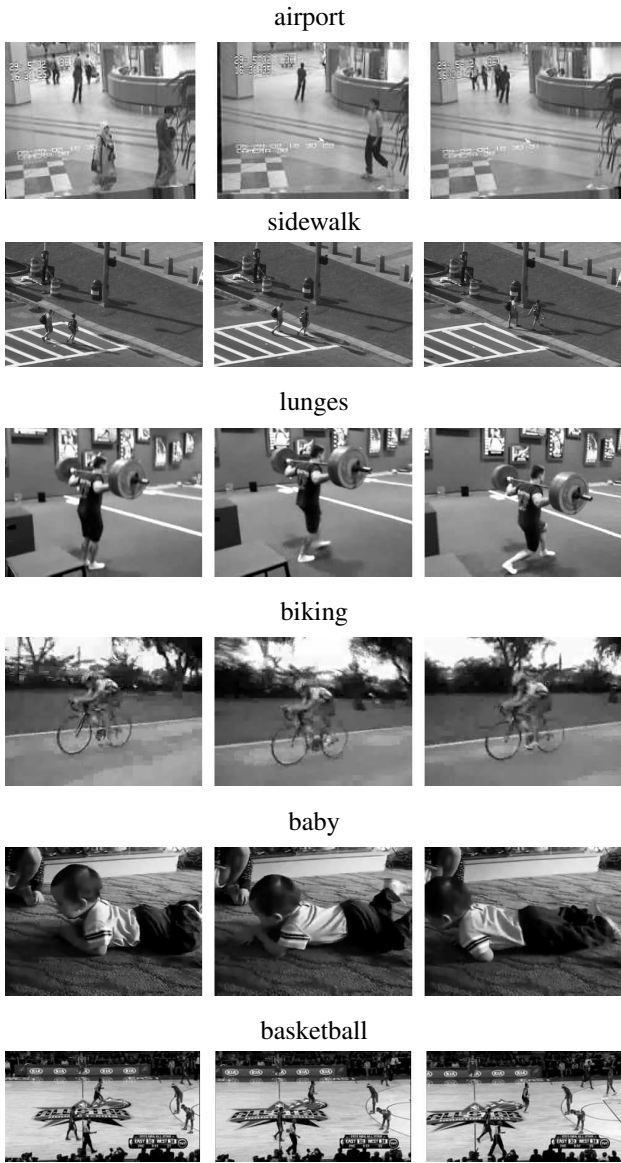


Fig. 7. Some frames of six videos under test.

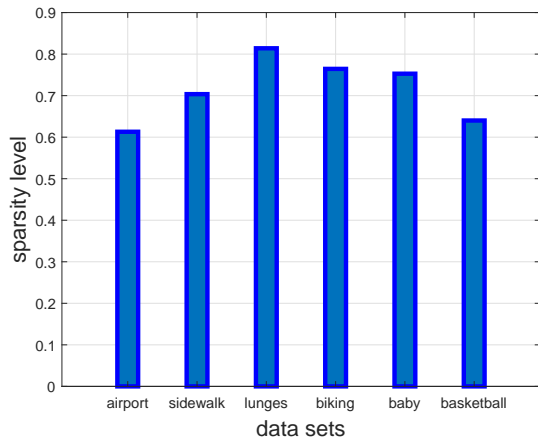


Fig. 8. Sparsity level of video data sets under DCT.

by different algorithms are displayed from the second row to the bottom. From the inpainted frames, it is obvious that both DCT-WNN and DCT-IpST can successfully obtain relatively ideal videos even for highly undersampled cases.

C. Discussion

Parameters sensitivity: Notice that there are some model parameters in our models, which are very important for the numerical performance of the models. However, it is well-known that setting model parameters is an incredibly difficult task in practice. Generally speaking, we can take constants empirically according to existing experiments in the literature. Here, we will conduct the numerical sensitivity of our models’ parameters. Note that there is a triple of parameters in model (9), i.e., $\{(\alpha_1, \dots, \alpha_N), \delta, \lambda\}$. According to [53], [58], we can easily determine the choice of α_i ’s. So, we below are concerned with the sensitivity of δ and λ . Similarly, for model (17), we focus on the sensitivity of p and λ . In our experiments, we consider the “airport” video data set with $sr = 30\%$. The parameter sensitivity results are summarized in Fig. 10. It can be easily seen from Fig. 10 that both models run relatively robust for $\lambda \in [0.01, 1]$, which also provides us some suggestions on the settings for the above experiments.

Model discussion: Notice that the objective functions of our models consists of two nonsmooth parts. Ones will be interested in what will happen if we remove one of the nonsmooth parts. To answer this question, we shall investigate the numerical performance of our models when removing the low-rank regularization term or the sparse term. Here, we also focus on the “airport” video data set with $sr = \{5\%, 10\%, 20\%, 30\%\}$ in our experiments. In Fig. 11, “only low-rank term” and “only sparse term” correspond to our models without sparse term and without low-rank regularization, respectively. From the plots in Fig. 11, we observe that our models equipped with only one low-rank term works better than the cases with only one sparse term. However, the proposed models with sparse and low-rank terms have the best numerical performance, which also sufficiently supports the idea of this paper.

In summary, the above computational results show that the proposed DCT-WNN and DCT-IpST are powerful to complete different types of downsampled images and videos data sets. Although our DCT-WNN and DCT-IpST cannot obtain the same inpainting quality of the state-of-the-art deep learning method DP3LRTC, DCT-WNN and DCT-IpST run much faster for large-scale data sets than DP3LRTC on a general personal computer. From the computing time and computer hardware perspectives, those model-driven approaches still have their own advantages. Moreover, we believe that our models could be further improved if some deep learning techniques are embedded in. We leave it as one of our future concerns.

V. CONCLUSION

In this paper, we introduced a unified “sparse + low-rank” tensor completion approach, which includes two structured optimization models for recovering images and videos from highly undersampled data. By introducing auxiliary variables,

TABLE II
 NUMERICAL RESULTS OF THE TEN ALGORITHMS FOR RECOVERING VIDEO DATA SETS.

Videos Datasets	Method	sr = 0.05			sr = 0.10			sr = 0.20			sr = 0.30		
		PSNR	SSIM	TIME(s)	PSNR	SSIM	TIME(s)	PSNR	SSIM	TIME(s)	PSNR	SSIM	TIME(s)
airport 144 × 176 × 30	IpST	17.62	0.371	16.68	19.6	0.485	14.01	22.23	0.661	12.41	24.32	0.778	10.64
	TTNNL1	17.98	0.499	19.81	20.06	0.499	19.14	22.74	0.672	18.42	24.68	0.777	18.48
	F-TNN	17.94	0.372	111.83	20.68	0.581	113.82	23.20	0.733	124.34	25.12	0.826	126.64
	TNN-3DTV	17.44	0.297	169.11	19.15	0.426	136.12	21.47	0.593	124.34	23.46	0.713	120.98
	TCTF	6.22	0.009	15.01	6.74	0.015	36.89	8.00	0.030	38.51	11.51	0.091	39.14
	WSTNN	18.78	0.4403	35.34	20.28	0.533	27.91	22.29	0.669	19.64	23.99	0.761	16.71
	SMF-LRTC	14.73	0.161	154.23	19.08	0.3967	183.62	23.25	0.685	196.20	24.93	0.763	210.60
	DP3LRTC	21.14	0.629	394.33	23.15	0.749	384.42	25.68	0.846	371.67	27.82	0.911	364.87
	DCT-IPST	18.79	0.416	33.25	20.75	0.520	34.04	22.98	0.660	35.40	24.65	0.749	34.59
	DCT-WNN	19.30	0.445	27.41	21.31	0.559	31.09	23.38	0.687	27.67	24.98	0.763	25.53
sidewalk 220 × 352 × 30	IpST	19.71	0.537	64.84	23.30	0.684	62.70	27.22	0.823	50.37	29.79	0.888	44.22
	TTNNL1	20.40	0.557	72.28	23.67	0.696	72.47	27.48	0.826	72.57	29.80	0.881	72.46
	F-TNN	20.12	0.551	478.43	21.47	0.581	475.44	24.08	0.721	467.23	26.27	0.800	462.11
	TNN-3DTV	19.35	0.463	567.70	21.17	0.567	462.03	23.76	0.691	307.24	26.00	0.781	253.84
	TCTF	6.22	0.013	121.53	9.36	0.019	121.11	13.39	0.114	129.77	18.58	0.410	121.26
	WSTNN	23.30	0.730	100.96	25.72	0.813	81.01	28.38	0.880	62.80	30.32	0.915	48.75
	SMF-LRTC	18.38	0.382	506.63	23.68	0.642	546.37	27.91	0.810	622.66	29.96	0.865	631.38
	DP3LRTC	23.83	0.749	1230.33	27.37	0.840	1273.42	30.57	0.906	1272.67	32.81	0.937	1215.87
	DCT-IPST	21.39	0.594	133.86	24.41	0.711	127.81	27.75	0.817	122.64	29.85	0.869	122.87
	DCT-WNN	22.04	0.624	106.72	25.14	0.740	105.36	28.31	0.833	109.45	30.29	0.880	110.15
basketball 144 × 256 × 30	IpST	15.16	0.324	29.98	17.08	0.451	27.26	19.81	0.632	23.11	21.90	0.751	19.97
	TTNNL1	15.95	0.405	31.87	18.32	0.570	28.33	21.21	0.704	27.76	23.37	0.808	28.21
	F-TNN	17.33	0.465	178.08	19.09	0.568	182.02	21.81	0.723	183.40	23.93	0.819	189.24
	TNN-3DTV	16.12	0.351	290.96	17.86	0.494	217.19	20.08	0.593	141.59	21.95	0.749	116.23
	TCTF	5.87	0.015	26.65	6.56	0.029	36.89	8.34	0.083	58.17	12.97	0.294	59.13
	WSTNN	16.49	0.430	45.76	19.02	0.566	46.02	21.29	0.702	28.76	23.31	0.797	23.99
	SMF-LRTC	14.36	0.216	221.59	17.75	0.403	251.97	20.88	0.609	284.98	22.73	0.717	306.55
	DP3LRTC	17.14	0.561	743.33	19.17	0.688	987.42	22.01	0.817	984.67	24.26	0.887	986.87
	DCT-IPST	16.89	0.421	52.67	20.75	0.559	53.45	22.10	0.708	53.15	24.03	0.786	56.45
	DCT-WNN	17.24	0.438	41.45	19.29	0.578	43.28	22.42	0.717	44.86	24.32	0.790	46.26
lunges 240 × 320 × 30	IpST	21.30	0.663	95.15	25.38	0.812	78.97	31.15	0.932	67.64	35.50	0.970	57.82
	TTNNL1	21.41	0.678	70.51	25.88	0.837	68.60	31.67	0.942	64.75	35.42	0.971	64.12
	F-TNN	23.33	0.809	448.61	25.60	0.867	456.51	28.91	0.922	460.82	31.70	0.950	462.13
	TNN-3DTV	22.70	0.777	784.30	25.41	0.864	565.78	29.04	0.926	386.18	32.19	0.957	310.20
	TCTF	6.37	0.011	58.18	7.45	0.021	58.39	12.54	0.245	59.79	20.92	0.511	60.19
	WSTNN	19.96	0.676	103.24	23.77	0.808	78.69	27.82	0.669	68.75	31.25	0.903	83.01
	SMF-LRTC	17.40	0.327	461.25	22.98	0.675	532.40	29.69	0.902	601.66	33.10	0.944	638.61
	DP3LRTC	24.55	0.873	1226.33	28.14	0.933	1340.42	32.71	0.971	1378.67	35.94	0.984	1347.87
	DCT-IPST	23.43	0.774	121.29	27.94	0.799	125.86	33.06	0.955	124.13	36.36	0.976	121.36
	DCT-WNN	24.25	0.799	105.47	29.19	0.911	110.56	34.18	0.963	115.50	37.29	0.979	118.03
biking 240 × 320 × 30	IpST	19.54	0.588	78.98	23.25	0.714	70.72	29.26	0.886	63.287	33.17	0.945	53.48
	TTNNL1	20.57	0.631	70.81	24.16	0.750	68.96	29.16	0.885	66.37	32.25	0.933	67.24
	F-TNN	20.81	0.640	455.86	22.83	0.701	457.11	26.15	0.809	463.97	28.77	0.878	464.76
	TNN-3DTV	19.06	0.529	741.98	22.08	0.659	575.65	25.88	0.804	412.79	28.89	0.884	324.97
	TCTF	7.44	0.011	15.01	8.23	0.016	36.89	12.86	0.181	38.51	17.18	0.500	39.14
	WSTNN	20.49	0.660	106.80	24.13	0.781	80.386	27.85	0.873	68.03	30.76	0.921	72.38
	SMF-LRTC	17.21	0.417	459.85	23.46	0.683	530.40	30.03	0.884	594.52	33.29	0.932	615.38
	DP3LRTC	25.17	0.829	1219.33	28.45	0.898	1217.42	31.80	0.946	1222.67	34.17	0.966	1211.87
	DCT-IPST	21.79	0.665	121.81	25.13	0.771	125.62	29.62	0.884	123.93	32.46	0.930	125.49
	DCT-WNN	22.44	0.693	104.37	26.17	0.810	108.59	30.55	0.905	115.97	33.23	0.942	115.84
baby 240 × 320 × 30	IpST	20.46	0.478	81.32	23.40	0.635	64.18	27.30	0.810	54.44	30.27	0.895	45.72
	TTNNL1	20.64	0.499	80.29	23.67	0.658	70.88	27.43	0.826	65.43	30.16	0.887	67.48
	F-TNN	21.32	0.542	503.42	23.13	0.631	454.69	25.96	0.757	463.50	28.16	0.835	462.16
	TNN-3DTV	20.50	0.467	758.46	22.83	0.610	463.90	25.90	0.758	336.95	28.35	0.845	266.91
	TCTF	8.19	0.011	51.14	9.29	0.020	59.54	13.23	0.179	60.43	19.95	0.477	60.94
	WSTNN	21.48	0.577	100.42	23.66	0.695	80.13	26.42	0.811	61.08	28.73	0.879	50.98
	SMF-LRTC	18.46	0.347	489.33	23.68	0.601	540.42	28.28	0.810	596.67	30.51	0.873	625.87
	DP3LRTC	24.60	0.723	1208.33	27.52	0.822	1213.42	31.05	0.909	1216.67	33.44	0.944	1237.87
	DCT-IPST	21.88	0.551	121.29	24.71	0.689	123.93	27.92	0.813	124.60	30.39	0.881	125.18
	DCT-WNN	22.63	0.592	102.43	25.49	0.729	105.54	28.68	0.839	112.11	31.13	0.898	112.27

we gainfully separated the two nonsmooth terms appeared in the objective functions, thereby being of benefit for designing easily implementable algorithms for the underlying separable models. A series of computational experiments on RGB images and surveillance videos data sets demonstrated that our approach performs better than some state-of-the-art model-driven tensor completion approaches.

Declaration of Competing Interest: The authors declared that

they have no known competing financial interests or personal relationships that could have appeared to influence the work reported in this paper.

ACKNOWLEDGMENTS

The authors are grateful to the editor and two anonymous referees for their close reading and valuable comments, which led to great improvements of the paper. They also would like to thank all authors of [12], [39], [44], [48], [50], [53], [58],

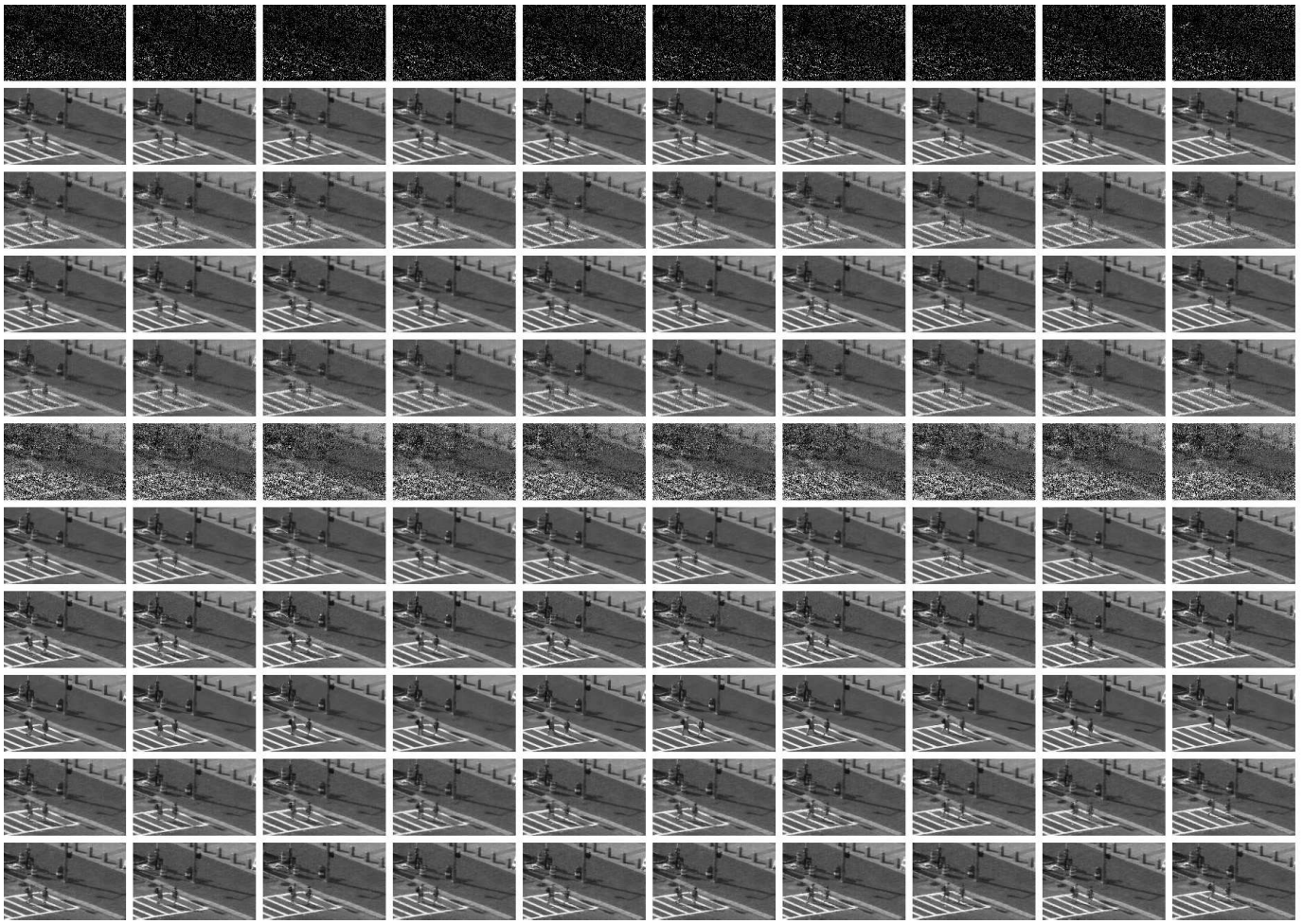


Fig. 9. Visualizations of recovered ‘sidewalk’ data sets by the ten algorithms. From left to right: ten consecutive observed frames with 20% information. From top to bottom: observed frames, and frames recovered by IpST, TTNL1, F-TNN, TNN-3DTV, TCTF, WSTNN, SMF-LRTC, DP3LRTC, DCT-IpST and DCT-WNN, respectively.

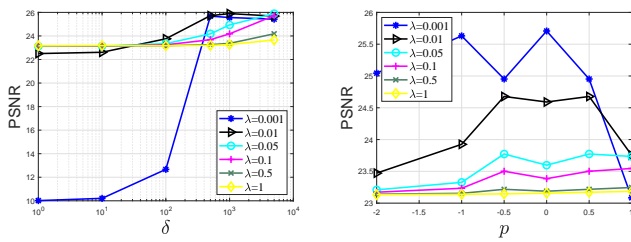


Fig. 10. Numerical sensitivity of model parameters λ , δ , and p . The left figure corresponds to our first model (9). The right one corresponds to the second model (17).

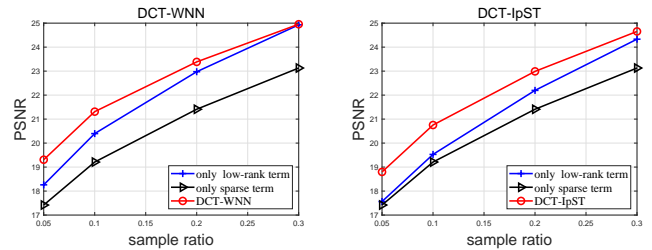


Fig. 11. Numerical performance of our models with only one low-rank objective or with only one sparse regularization term, respectively.

[59] for sharing their code, especially thank Dr. Yufan Li and Mr. Zhiyuan Zhang for their kind help on our experiments. C. Ling and H. He were supported in part by National Natural Science Foundation of China (Nos. 11971138 and 11771113) and Natural Science Foundation of Zhejiang Province (Nos. LY19A010019 and LD19A010002).

REFERENCES

[1] N. Komodakis, “Image completion using global optimization,” in *Computer Vision and Pattern Recognition*, vol. 1, 2006, pp. 442–452.

[2] N. Hao, M. Kilmer, K. Braman, and R. Hoover, “Facial recognition using tensor-tensor decompositions,” *SIAM J. Imaging Sci.*, vol. 6, no. 1, pp. 437–463, 2013.

[3] A. Criminisi, P. Perez, and K. Toyama, “Region filling and object removal by exemplar-based image inpainting,” *IEEE Trans. Image Process.*, vol. 13, no. 9, pp. 1200–1212, 2004.

[4] X. Geng, K. Smith-Miles, Z. Zhou, and L. Wang, “Face image modeling by multilinear subspace analysis with missing values,” *Proceedings of the 17th ACM international conference on Multimedia*, 2009.

[5] A. Efros and T. Leung, “Texture synthesis by non-parametric sampling,” in *Computer Vision, 1999. The Proceedings of the Seventh IEEE International Conference on*, 1999, pp. 1033–1038.

[6] D. Coupier, A. Desolneux, and B. Ycart, “Image denoising by statistical

- area thresholding,” in *Mustererkennung, 21 Dagm-symposium, Bonn, September, 1999*.
- [7] G. Golub and C. Van Loan, *Matrix Computations*, 4th ed. Baltimore: The Johns Hopkins University Press, 2013.
- [8] Q. Song, H. Ge, J. Caverlee, and X. Hu, “Tensor completion algorithms in big data analytics,” *ACM Trans. Knowl. Discovery Data*, vol. 13, pp. 1–48, 2019.
- [9] J. Liu, P. Musialski, P. Wonka, and J. Ye, “Tensor completion for estimating missing values in visual data,” *IEEE Trans. Pattern Anal. Mach. Intell.*, vol. 35, no. 1, pp. 208–220, 2013.
- [10] S. Gandy, B. Recht, and I. Yamada, “Tensor completion and low-rank tensor recovery via convex optimization,” *Inverse Probl.*, vol. 27, p. 025010, 2011.
- [11] C. Lu, J. Feng, Z. Lin, and S. Yan, “Exact low tubal rank tensor recovery from Gaussian measurements,” in *Proceedings of the Twenty-Seventh International Joint Conference on Artificial Intelligence, IJCAI-18*. International Joint Conferences on Artificial Intelligence Organization, 7 2018, pp. 2504–2510.
- [12] P. Zhou, C. Lu, Z. Lin, and C. Zhang, “Tensor factorization for low-rank tensor completion,” *IEEE Trans. Image Process.*, vol. 27, no. 3, pp. 1152–1163, 2018.
- [13] Y. Chen, C. Hsu, and H. Liao, “Simultaneous tensor decomposition and completion using factor priors,” *IEEE Trans. Pattern Anal. Mach. Intell.*, vol. 36, no. 3, pp. 577–591, 2014.
- [14] E. Candès and B. Recht, “Exact matrix completion via convex optimization,” *Found. Comput. Math.*, vol. 9, no. 6, pp. 717–772, 2009.
- [15] C. Hillar and L. Lim, “Most tensor problems are NP-hard,” *J. ACM*, vol. 6, pp. 1–39, 2013.
- [16] T. Kolda and B. Bader, “Tensor decompositions and applications,” *SIAM Rev.*, vol. 51, pp. 455–500, 2009.
- [17] I. Oseledets, “Tensor-train decomposition,” *SIAM J. Sci. Comput.*, vol. 33, no. 5, pp. 2295–2317, 2011.
- [18] T. Jiang, T. Huang, X. Zhao, T. Ji, and L. Deng, “Matrix factorization for low-rank tensor completion using framelet prior,” *Inf. Sci.*, vol. 436–437, pp. 403–417, 2018.
- [19] K. Hosono, S. Ono, and T. Miyata, “Weighted tensor nuclear norm minimization for color image denoising,” in *2016 IEEE International Conference on Image Processing (ICIP)*, 2016, pp. 3081–3085.
- [20] L. Huang, H. So, Y. Chen, and W. Wang, “Truncated nuclear norm minimization for tensor completion,” in *IEEE Sensor Array and Multichannel Signal Processing Workshop*, 2014.
- [21] J. Bengua, H. Phien, H. D. Tuan, and M. Do, “Efficient tensor completion for color image and video recovery: Low-rank tensor train,” *IEEE Trans. Image Process.*, vol. 26, no. 5, pp. 2466–2479, 2017.
- [22] T. Y. Ji, T. Z. Huang, X. L. Zhao, T. H. Ma, and G. Liu, “Tensor completion using total variation and low-rank matrix factorization,” *Inf. Sci.*, vol. 326, pp. 243–257, 2016.
- [23] J. Xue, Y. Zhao, W. Liao, and J. C. Chan, “Nonconvex tensor rank minimization and its applications to tensor recovery,” *Inf. Sci.*, vol. 503, pp. 109–128, 2019.
- [24] Z. Zhang and S. Aeron, “Exact tensor completion using t-SVD,” *IEEE Trans. Signal Process.*, vol. 65, no. 6, pp. 1511–1526, 2017.
- [25] C. Lu, J. Feng, Y. Chen, W. Liu, Z. Lin, and S. Yan, “Tensor robust principal component analysis: Exact recovery of corrupted low-rank tensors via convex optimization,” *2016 IEEE Conference on Computer Vision and Pattern Recognition (CVPR)*, pp. 5249–5257, 2016.
- [26] C. Lu, J. Feng, Y. Chen, W. Liu, Z. Lin, and S. Yan, “Tensor robust principal component analysis with a new tensor nuclear norm,” *IEEE Trans. Pattern Anal. Mach. Intell.*, vol. 42, pp. 925–938, 2020.
- [27] M. Yuan and C. Zhang, “On tensor completion via nuclear norm minimization,” *Found. Comput. Math.*, vol. 16, pp. 1031–1068, 2016.
- [28] M. Kilmer and C. Martin, “Factorization strategies for third-order tensors,” *Linear Algebra Appl.*, vol. 435, no. 3, pp. 641–658, 2011.
- [29] Q. Zhao, L. Zhang, and A. Cichocki, “Bayesian CP factorization of incomplete tensors with automatic rank determination,” *IEEE Trans. Pattern Anal. Mach. Intell.*, vol. 37, no. 9, pp. 1751–1763, 2015.
- [30] M. Filipović and A. Jukić, “Tucker factorization with missing data with application to low-n-rank tensor completion,” *Multidim. Syst. Sign. Process.*, vol. 26, no. 3, pp. 677–692, 2015.
- [31] T. Yokota, Q. Zhao, and A. Cichocki, “Smooth PARAFAC decomposition for tensor completion,” *IEEE Trans. Signal Process.*, vol. 64, no. 20, pp. 5423–5436, 2016.
- [32] Y. Wu, H. Tan, Y. Li, J. Zhang, and X. Chen, “A fused CP factorization method for incomplete tensors,” *IEEE Trans. Neural. Netw. Learn. Syst.*, vol. 30, no. 3, pp. 751–764, 2019.
- [33] X. Lin, M. Ng, and X. Zhao, “Tensor factorization with total variation and tikhonov regularization for low-rank tensor completion in imaging data,” *J. Math. Imaging Vis.*, vol. 62, pp. 900–918, 2020.
- [34] Y. Liu, F. Shang, W. Fan, J. Cheng, and H. Cheng, “Generalized higher order orthogonal iteration for tensor learning and decomposition,” *IEEE Trans. Neural. Netw. Learn. Syst.*, vol. 27, no. 12, pp. 2551–2563, 2016.
- [35] L. Rudin, S. Osher, and E. Fatemi, “Nonlinear total variation based noise removal algorithms,” *Physica D*, vol. 60, pp. 227–238, 1992.
- [36] V. Varghees, M. Manikandan, and R. Gini, “Adaptive mri image denoising using total-variation and local noise estimation,” in *Proceedings of the 2012 International Conference on Advances in Engineering, Science and Management (ICAESM)*, 2012, pp. 506–511.
- [37] M. Qin, Z. Li, S. Chen, Q. Guan, and J. Zheng, “Low-rank tensor completion and total variation minimization for color image inpainting,” *IEEE Access*, vol. 8, pp. 53 049–53 061, 2020.
- [38] X. Zhao, X. Nie, Y. Zheng, T. Ji, and T. Huang, “Low-rank tensor completion via tensor nuclear norm with hybrid smooth regularization,” *IEEE Access*, vol. 7, pp. 131 888–131 901, 2019.
- [39] F. Jiang, X. Liu, H. Lu, and R. Shen, “Anisotropic total variation regularized low-rank tensor completion based on tensor nuclear norm for color image inpainting,” in *2018 IEEE International Conference on Acoustics, Speech and Signal Processing (ICASSP)*, 2018, pp. 1363–1367.
- [40] D. Qiu, M. Bai, M. Ng, and X. Zhang, “Robust low-rank tensor completion via transformed tensor nuclear norm with total variation regularization,” *Neurocomputing*, vol. 435, pp. 197–215, 2021.
- [41] Y. Wang, C. Xu, S. You, C. Xu, and D. Tao, “DCT-regularized extreme visual recovery,” *IEEE Trans. Image Process.*, vol. 26, pp. 3360–3371, 2018.
- [42] Y. Abe and Y. Iguni, “Image restoration from a downsampled image by using the DCT,” *Signal Processing*, vol. 87, pp. 2370–2380, 2007.
- [43] Y. Du, G. Han, Y. Quan, Z. Yu, H. Wong, C. L. P. Chen, and J. Zhang, “Exploiting global low-rank structure and local sparsity nature for tensor completion,” *IEEE Trans. Cybern.*, vol. 49, no. 11, pp. 3898–3910, 2019.
- [44] Z. Han, C. Leung, L. Huang, and H. So, “Sparse and truncated nuclear norm based tensor completion,” *Neural Process. Lett.*, vol. 45, pp. 729–743, 2017.
- [45] Y. Li, L. Shen, and B. Suter, “Adaptive inpainting algorithm based on DCT induced wavelet regularization,” *IEEE Trans. Image Process.*, vol. 22, pp. 752–763, 2013.
- [46] B. Madathil and S. George, “DCT based weighted adaptive multi-linear data completion and denoising,” *Neurocomputing*, vol. 318, pp. 120–136, 2018.
- [47] Y. Wang and Q. Zhu, “Signal loss recovery in DCT-based image and video codecs,” in *Visual Communications and Image Processing ’91: Visual Communication*, K.-H. Tzou and T. Koga, Eds., vol. 1605, International Society for Optics and Photonics. SPIE, 1991, pp. 667–678.
- [48] T. Jiang, M. Ng, X. Zhao, and T. Huang, “Framelet representation of tensor nuclear norm for third-order tensor completion,” *IEEE Trans. Image Process.*, vol. 29, pp. 7233–7244, 2020.
- [49] T. Jiang, X. Zhao, H. Zhang, and M. Ng, “Dictionary learning with low-rank coding coefficients for tensor completion,” *IEEE Trans. Neural. Netw. Learn. Syst.*, 2021.
- [50] X. Zhao, W. Xu, T. Jiang, Y. Wang, and M. Ng, “Deep plug-and-play prior for low-rank tensor completion,” *Neurocomputing*, vol. 400, pp. 137–149, 2020.
- [51] R. Chartrand, “Shrinkage mappings and their induced penalty functions,” in *2014 IEEE International Conference on Acoustics, Speech and Signal Processing (ICASSP)*, 2014, pp. 1026–1029.
- [52] R. Chartrand, “Fast algorithms for nonconvex compressive sensing: MRI reconstruction from very few data,” in *2009 IEEE International Symposium on Biomedical Imaging: From Nano to Macro*, 2009, pp. 262–265.
- [53] K. Shang, Y. Li, and Z. Huang, “Iterative p-shrinkage thresholding algorithm for low Tucker rank tensor recovery,” *Inf. Sci.*, vol. 482, pp. 374–391, 2019.
- [54] S. Gaïffas and G. Lecué, “Weighted algorithms for compressed sensing and matrix completion,” 2011, <https://arxiv.org/abs/1107.1638>.
- [55] C. Lu, J. Tang, S. Yan, and Z. Lin, “Nonconvex nonsmooth low rank minimization via iterative reweighted nuclear norm,” *IEEE Trans. Image Process.*, vol. 25, pp. 829–839, 2016.
- [56] J. Woodworth and R. Chartrand, “Compressed sensing recovery via nonconvex shrinkage penalties,” *Inverse Probl.*, vol. 32, pp. 075004, 2016.

- [57] T. Oh, Y. Tai, J. Bazin, H. Kim, and I. Kweon, "Partial sum minimization of singular values in robust PCA: Algorithm and applications," *IEEE Trans. Image Process.*, vol. 38, pp. 744–758, 2016.
- [58] Y. Zheng, T. Huang, X. Zhao, T. Jiang, and T. Ma, "Tensor n-tubal rank and its convex relaxation for low-rank tensor recovery," *Information Sciences.*, vol. 532, pp. 170–189, 2020.
- [59] Y. Zheng, T. Huang, T. Ji, X. Zhao, T. Jiang, and T. Ma, "Low-rank tensor completion via smooth matrix factorization," *Appl. Math. Model.*, vol. 70, pp. 677–695, 2019.
- [60] Z. Wang, A. Bovik, H. Sheikh, E. Simoncelli, "Image quality assessment: From error visibility to structural similarity", *IEEE Trans. Image Process.*, vol. 13, pp. 600–612, 2004.